Tunnelling and Underground Space Technology 106 (2020) 103588

Contents lists available at ScienceDirect

Tunnelling and Underground Space Technology

journal homepage: www.elsevier.com/locate/tust

Algorithm for generation of 3D polyhedrons for simulation of rock particles by DEM and its application to tunneling in boulder-soil matrix

Shuaiwen Cui[a], Yong Tan[a,*], Ye Lu[b]

[a] Dept. of Geotechnical Engineering, College of Civil Engineering, Tongji Univ., 1239 Siping Rd., Shanghai 200092, PR China
[b] Dept. of Civil Engineering, Shanghai Univ., 99 Shang-Da Rd., Shanghai 200444, PR China

ARTICLE INFO

Keywords:
Polyhedron generation
Rock particle simulation
Convexity control
GJK algorithm
Tunneling
Boulder-soil matrix

ABSTRACT

The shape of rock particle can profoundly affect its mechanical behaviors due to the interlocking force associated with morphological features. In this study, a hybrid extension method encompassing both convexity control and overlap detection was developed to generate three-dimensional (3D) polyhedrons for simulating irregularly shaped rock particles by discrete-element-method (DEM). Based on a random initial tetrahedron, a polyhedron can be extended from a simple shape to a complex one by adding new tetrahedrons. To control polyhedron convexity, a two-step method derived from the definition of convexity was proposed in this study. Moreover, the enhanced Gilbert–Johnson–Keerthi (GJK) algorithm was applied for overlap detection during the extension process of polyhedron generation. With the proposed hybrid extension method (HEM), a numerical model for simulation of tunnelling in boulder-soil matrix was built in the commercial DEM software; then, extensive parametric studies were performed to explore the influence of several factors (boulder size, orientation, position, and morphology) on tunnelling. The simulation results demonstrate the efficiency and reliability of the proposed algorithm and revealed the ground movement patterns in case an undetected large boulder was accidently encountered by tunnelling at shallow depth.

1. Introduction

Granular materials (gravels, cobbles, pebbles, boulders, and soil-rock mixture) are widely encountered in tunneling and other civil engineering projects (Long et al., 2012; Tan et al., 2018). Due to their irregular shapes, interlocking force exists among granular particles (Ting et al., 1995; Latham et al., 2008; Lu et al., 2017). Relevant studies in literature have demonstrated that the shapes of granular materials have significant effects on their mechanical behaviors (Evans and Frost, 2010; Jin et al., 2016; Lu et al., 2018; Zhou et al., 2019). Thereby, it is essential to account for the particle shape effect in design or analysis of construction executed in soil-rock mixed strata. Disregarding this effect in design or analysis may lead to accidents or unnecessary economic waste.

Concerning the investigation of particle shape effect, physical modeling and numerical simulation are two popular alternatives. Physical modeling is commonly time-consuming and expensive; meanwhile, its reliability is affected by experimental conditions to some extent. Since numerical simulation features great flexibility for loading configuration, physical properties of the material, and so on, it is more suitable for simulating the particle shape effect and interpreting mechanical behaviors from a mesoscopic perspective (Evans et al., 2009; Li and Wang, 2017; Ngo et al., 2014). Moreover, numerical simulation data can be accessible at any stage.

To date, numerical modeling is usually performed by a continuous or discontinuous simulation approach. Compared with the continuous simulation methods (finite element method - FEM, finite difference method – FDM, and boundary element method - BEM), the discontinuous methods, including discrete element method - DEM (Cundall, 1971), discontinuous deformation analysis - DDA (Shi, 1992) and key block theory - KBT (Shi and Goodman, 1989), are more suitable for simulation of granular materials because of their discrete nature. Different from DDA and KBT developed for rock blocks, DEM (Cundall and Strack, 1979) is more suitable for simulation of granular materials. Furthermore, DEM can simulate particle shapes, multi-field coupling, and etc. Thereby, DEM is an appropriate tool for simulating irregularly shaped granular materials. Currently, granular materials are commonly simplified in most DEM softwares as disks in two-dimension (2D) or spheres in three-dimension (3D) for simulation, ignoring their morphological features and interlocking force. As mentioned previously, interlocking force among granular particles is governed by particle shapes. Therefore, a method, which can simulate irregular shapes of

* Corresponding author.
E-mail addresses: 1832485@tongji.edu.cn (S. Cui), tanyong21th@tongji.edu.cn (Y. Tan), ye.lu@shu.edu.cn (Y. Lu).

https://doi.org/10.1016/j.tust.2020.103588
Received 30 November 2019; Received in revised form 19 August 2020; Accepted 23 August 2020
Available online 02 September 2020
0886-7798/ © 2020 Elsevier Ltd. All rights reserved.

Nomenclature

A	the vertex A
B	the vertex B
C	the vertex C
C_e	the centroid of facet BCD
C_f	the centroid of facet ABD
$CS(OBJ1, OBJ2)$	the contact state of $OBJ1$ and $OBJ2$.
D	the vertex D
DS	the domain space
E	the vertex generated by the improved REM
E'	the intersection point of the ray (OC_e) and the spherical surface
$E(e)$	the index indicating the extension degree in the iteration of a vertex (e.g. E)
F	the vertex generated by the improved PEM
$F(i, r)$	the user-customized control function of extension degree
$MDS(SP_A, SP_B)$	the space occupied by the Minkowski difference of SP_A and SP_B
$MTD(SP_A, SP_B)$	the minimum translation distance of SP_A and SP_B
Num	the number of vertices of a polyhedron
O	the origin
$OBJ1$	the first object to be investigated in overlap detection
$OBJ2$	the second object to be investigated in overlap detection
OC_e	the ray OC_e
R_e	the radius of the minimal circumcircle of facet BCD
R_f	the radius of the minimal circumcircle of facet ABD
SN	the turning point of REM and PEM in HEM
SP_A	the space occupied by
SP_B	the space occupied by $OBJ2$
V	vertex V
V_{ABCD}	volume of the initial tetrahedron ($ABCD$)
V_{OABC}	volume of the tetrahedron ($OABC$)
V_{OABD}	volume of the tetrahedron ($OABD$)
V_{OACD}	volume of the tetrahedron ($OACD$)
V_{OBCD}	volume of the tetrahedron ($OBCD$)
V_f	the farthest point along the direction η
V_i	the vertex V_i
V_Ω	the volume of a polyhedron
X	the content of a sign function $sign(X)$
X_d	the distance TBM advanced
a_i	one of the coefficients of a facet (e.g. LMN)
a_{ij}	one of the coefficients of a facet (e.g. LMV_i, MNV_i, and NLV_i)
b_i	one of the coefficients of a facet (e.g. LMN)
b_{ij}	one of the coefficients of a facet (e.g. LMV_i, MNV_i, and NLV_i)
c_i	one of the coefficients of a facet (e.g. LMN)
c_{ij}	one of the coefficients of a facet (e.g. LMV_i, MNV_i, and NLV_i)
d_i	one of the coefficients of a facet (e.g. LMN)
d_{ij}	one of the coefficients of a facet (e.g. LMV_i, MNV_i, and NLV_i)
h_e	the distance from the new vertex (e.g.E) to its basic facet
i	the current iteration number
lb	the lower boundary of the range of ω
r	the retry number in an extension iteration
$spf_{DS}(\eta)$	the support function in DS with a given direction η
$spf_{MDS}(\eta)$	the support function in MDS with a given direction η
$spf_{SP_A}(\eta)$	the support function in SP_A with a given direction η
$spf_{SP_B}(\eta)$	the support function in SP_B with a given direction η
$spp_{DS}(\eta)$	the support function in with a given direction η
$spp_{MDS}(\eta)$	the support function in MDS with a given direction η
$spp_{SP_A}(\eta)$	the support function in SP_A with a given direction η
$spp_{SP_B}(\eta)$	the support function in SP_B with a given direction η
lb	the upper boundary of the range of ω
$\sum V_V$	the sum of oriented volumes formed by new vertex V and the existing facets
$\partial(SP_A)$	the boundary of SP_A
$\partial(SP_B)$	the boundary of SP_B
η	the direction for iteration in the enhanced GJK algorithm for overlap detection
η_0	the initial η
ω	the volume ratio of the initial tetrahedron to the unit sphere

particles in DEM, is essential for achieving reasonable simulation of mechanical behaviors of granular materials during construction (e.g., tunneling in boulder-soil mixtures).

To simulate morphological features, irregularly shaped particles can be reconstructed by assembling disks or spheres in DEM. This can be achieved by using several reconstruction algorithms available in literature, such as the surface normal method (Ferellec and McDowell, 2008), the bubble pack method (Taghavi, 2011), and medial-axis-oriented disk-laying approach (Lu et al., 2017). However, before reconstruction of irregularly shaped particles, particle shapes need to be obtained or generated first to serve as templates, which are to be filled by disks or spheres. This raises the problem of how to acquire random particle shapes with appropriate methods.

Currently, several methods for acquiring particle shapes have been proposed, which can be divided into image analysis methods and shape generation algorithms. The image analysis methods are based on realistic shapes of granular materials, e.g., grayscale analysis (Huang and Tutumluer, 2013), X-ray computed tomography (CT) (Lanaro and Tolppanen, 2002), and 3D laser scanning (Latham et al., 2008). These methods can capture realistic particle shapes, but are limited by the cost and repetitive work. Regarding shape generation algorithms, 2D algorithms (Wittmann et al., 1985; Du et al., 2013; Lu et al., 2017; Wang et al., 2019a) are more widely developed than 3D ones due to the simplicity of calculation and application. However, 2D algorithms are unable to solve non-planar problems.

Based on different mathematical principles, several 3D algorithms have been developed in recent years. However, some issues still remain to be solved. Eliáš (2014) adopted scattered nuclei to form 3D polyhedrons by using Voronoi tessellation. Since only the Voronoi cell associated with the central nucleus was used, just convex polyhedrons could be generated. Alternatively, using scattered points on a closed surface can also be used to generate polyhedrons. Since the clump templates in DEM softwares (e.g. PFC 5.0) are usually defined by nodes, edges, and facets (Itasca Consultant Group, 2015), knowledge of the connection of those points are required. To solve this issue, vertices are usually derived from the nodes of grids on a closed surface by allowing the nodes to change their coordinates within a prescribed area, which leads to limited randomness of vertices (Jin et al., 2016). A third choice is using the intersection of a set of half-spaces (Lee et al., 2009), which has been widely used in block generation procedures (Heliot, 1988; Zhang and Lei, 2013). Unlike granules, blocks are usually generated sequentially along with the generation of fractures for simulating tectonic processes, which explains why these methods are usually based on inequalities or half-spaces. With a contact detection algorithm (Boon et al., 2012) based on linear programming and the concept of analytic centre, Boon et al. (2015) used an effective one-level data structure consisting of the block faces, instead of a conventional 3-level data structure (face-vertex-edge), to generate rock mass. For generation of rock mass, these face-based methods are very effective. However, regarding granule simulation in DEM, particle templates are usually

defined by nodes and edges; hence, vertex-based algorithms will be preferred, e.g., the extension method. Instead of using a face-based structure, the extension method adopts a vertex-based data structure (vertex-edge-face) and a simple mathematic principle (vertex extension by iteration). Du et al. (2013) and Guo et al. (2017) developed the plane extension method (PEM) and ray extension method (REM), respectively. To apply the extension method, convexity control and overlap detection in the iteration are of vital importance; however, these two issues have not been solved satisfactorily. The REM (Guo et al., 2017) was a primitive idea without convexity control or overlap detection at all. Because of its deterministic procedures, REM has high computational efficiency but limited randomness. In PEM (Du et al., 2013), the convexity was checked by the oriented volume formed by the new vertex and the existing facets. However, it only ensured that the new vertex was generated outside the existing part without providing strict convexity. Moreover, collision detection in PEM was achieved by comparing $\sum V_V$ and V_Ω, where $\sum V_V$ denotes the sum of oriented volumes formed by new vertex V and the plane elements and V_Ω denotes the polyhedron volume. However, a line-facet intersection checking method has to be used in PEM as a supplement to avoid special cases.

Based on the technical concerns above, a hybrid extension method (HEM), which combines the merits of REM and PEM, was proposed in this study. To cope with the situations where polyhedron convexity was required, a two-step convexity control method was developed herein, which could strictly control convexity and ensure no overlap without using overlap detection. Regarding the situations where convexity was not required, the enhanced Gilbert–Johnson–Keerthi (GJK) algorithm (Gilbert et al., 1988) was incorporated into the proposed HEM for detecting overlap in diverse situations, which can overcome the problem in PEM. Finally, numerical simulations were conducted to validate the proposed algorithm and explore the influence of some major factors of boulder (size, orientation, position, and shape) on the tunnelling-boulder interaction. The simulation results showed that the size of ground influence zone and ground heave due to tunnelling-boulder interaction are closely related to boulder size, boulder burial depth and the distance from boulder to the centroid of cutterhead of tunnel boring

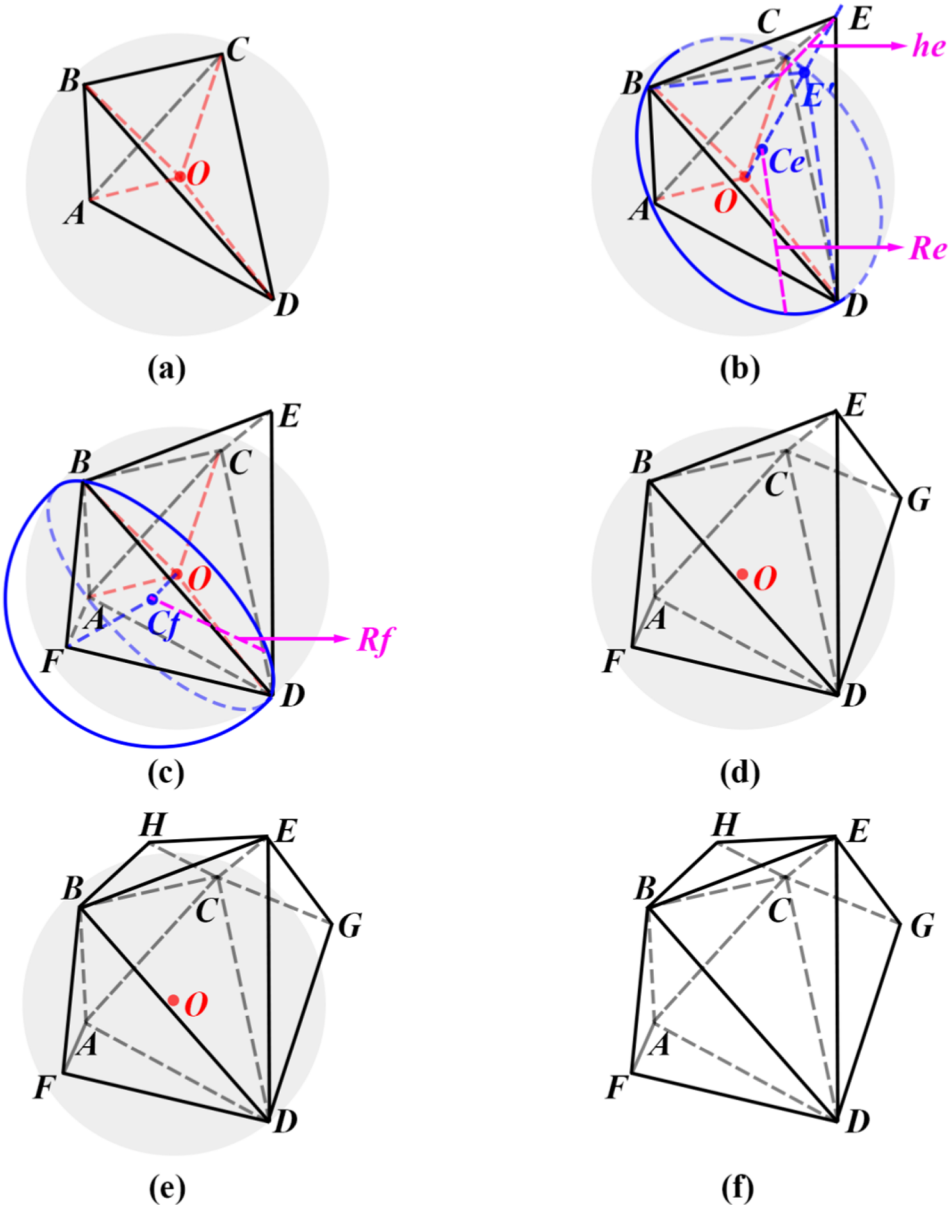


Fig. 1. Schematic illustration of the polyhedron extension process by the proposed hybrid extension method (HEM): (a) generation of the initial tetrahedron (*ABCD*); (b) vertex *E* generated by the improved ray extension method (REM) and vertex *E*′ generated by the original REM; (c) vertex *F* generated by the plane extension method (PEM); (d-e) iterations by the improved REM or PEM; and (f) the final polyhedron (*ABCDEFGH*).

machine (TBM). The distribution of ground influence zone was consistent with the trajectory of boulder encountered in tunnelling and the latter was sensitive to boulder position. Additionally, the boulder movement, in particular its rotation, was sensitive to its orientation and morphology. The simulation results indicated that if an undetected large isolated boulder was encountered by TBM tunnelling at shallow depth, it would incur adverse effects on the ground and even catastrophic ground failure, which should receive adequate attention in practice.

2. Hybrid extension method

The extension methods (REM and PEM), are able to extend an initial polyhedron (e.g. a tetrahedron) to a more complex one by iterations (Fig. 1). In this proposed method, the basic procedure is to choose a triangular facet from the current polyhedron and then add a new tetrahedron to it, which is repeated in each iteration until the requirements are fulfilled.

2.1. Initial tetrahedron

As shown in Fig. 1(a), to apply the extension method, a unit sphere needs to be generated first. Then, four random points (A, B, C, and D) on the spherical surface are selected to form an initial tetrahedron. Some subsequent procedures are based on the assumption that the origin (O) is inside the tetrahedron (excluding the surface). If the origin (O) was outside the tetrahedron, the initial tetrahedron needed to be regenerated. This can be expressed as follows:

$$V_{ABCD} = V_{OABC} + V_{OABD} + V_{OACD} + V_{OBCD}$$

$$V_{OABC} > 0,\ V_{OABD} > 0,\ V_{OACD} > 0,\ V_{OBCD} > 0 \quad (1)$$

where, V_{ABCD} = volume of the initial tetrahedron ($ABCD$); V_{OABC} = volume of the tetrahedron ($OABC$); V_{OABD} = volume of the tetrahedron ($OABD$); V_{OACD} = volume of the tetrahedron ($OACD$); V_{OBCD} = volume of the tetrahedron ($OBCD$).

To control the volume of an initial tetrahedron, the volume ratio, ω, of the initial tetrahedron to the unit sphere was introduced herein. As the initial tetrahedron was generated randomly, ω should be controlled within a suitable range. This can be expressed as $\omega \in [lb, ub]$ and the available range of ω is shown in formula (2) as below:

$$0 < lb \le \omega \le ub \le \frac{2\sqrt{3}}{9\pi}\left(\omega = \frac{3V_{ABCD}}{4\pi}\right) \quad (2)$$

where, the maximum value = $2\sqrt{3}/(9\pi)$ ($\approx$ 0.1225) indicates the volume ratio of a regular tetrahedron to the unit sphere.

It was revealed that with the two-step convexity control method (refer to the later Section 2.3), the shape of a convex polyhedron has a strong relationship with the sphericity (Barrett, 1980) of its initial tetrahedron. Thereby, the sphericity was mainly controlled by ω. A large ω is likely to result in large sphericity of an initial tetrahedron, which may further lead to a compact (equant) polyhedron. On the contrary, a small ω may result in small sphericity of an initial tetrahedron and further incur a platy or elongated polyhedron.

2.2. Extension procedure

After generation of the initial tetrahedron ($ABCD$), an iterative process was performed for extension. Since the proposed HEM is based on REM and PEM with improvements, the procedures of REM and PEM will be outlined first as below:

2.2.1. REM

As shown in Fig. 1(b), the procedures of REM (Guo et al., 2017) can be outlined as:

Step (1) - Choosing a triangular facet (BCD).
Step (2) - Obtaining the centroid (C_e) of BCD.
Step (3) - Obtaining a ray (OC_e) from the origin (O) and through C_e.
Step (4) - Calculating the intersection point (E') of the ray (OC_e) and the spherical surface.

This process is a deterministic one. Thus, there will be no overlap in the extension process. If there were enough vertices, the final polyhedron generated by REM would be inappropriate for representing a particle. Because it is difficult to generate a new vertex within the area behind the edges of the initial tetrahedron, the new vertex (E) was allowed to stochastically move along the ray (OC_e) within a prescribed range for increasing randomness (Fig. 1b). It should be pointed out that this improvement changed the deterministic nature of REM. Thus, the technical issues of convexity control and overlap detection were raised, which would be solved in Sections 2.3 and 2.4, respectively. With the improvement, steps (5–7) can be added as follows:

Step (5) - Obtaining point (E) by stochastically moving E' along the ray (OC_e) within the given range.
Step (6) - Checking whether E fulfills the requirements (e.g. convexity, no overlap, and extension degree) or not. If it does, go to step (7); otherwise, update the retry number ($r = r + 1$) and then return to step (5).
Step (7) - Adding E to the current polyhedron, and updating vertices, edges, facets, and the number of current iteration ($i = i + 1$).

2.2.2. PEM

As shown in Fig. 1(c), the procedures of PEM (Du et al., 2013) can be outlined as:

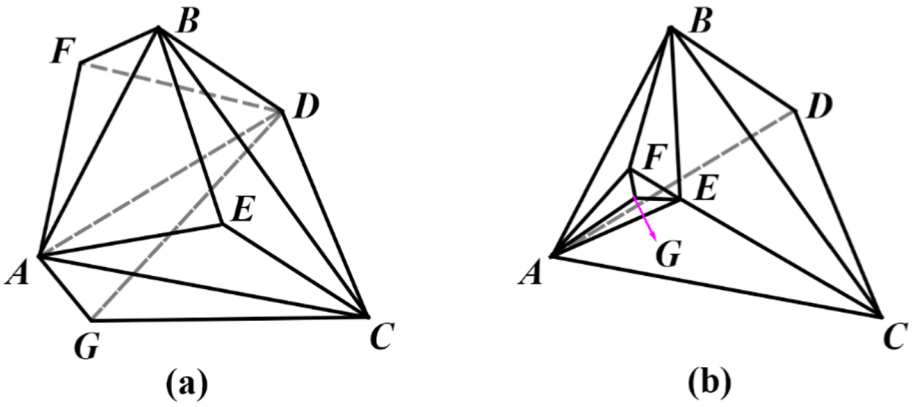


Fig. 2. New polyhedrons generated by the extension method using its: (a) largest circumcircle radius; and (b) shortest circumcircle radius.

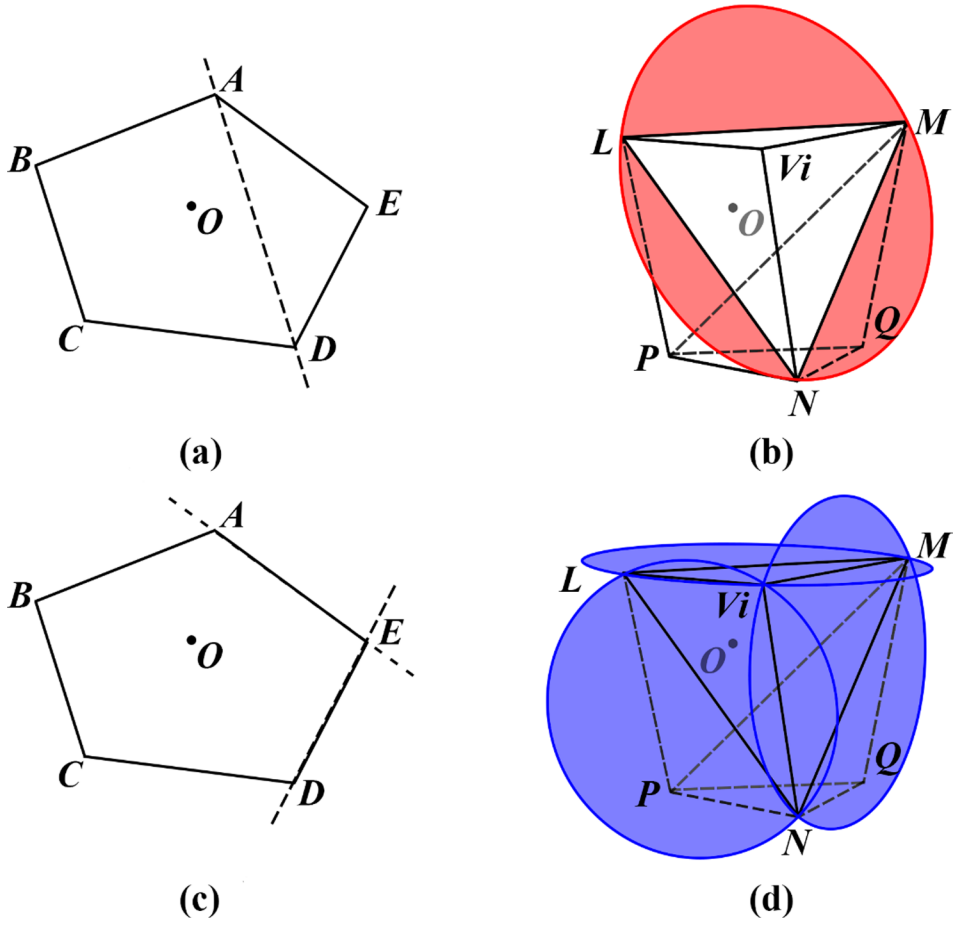


Fig. 3. Convexity control for each extension iteration by checking whether: (a-b) the new vertex $E(V_i)$ is outside the existing part of the polygon (polyhedron) or not; and (c-d) the entire polygon (polyhedron) is encompassed in the corner formed by the 2 new edges (3 new facets) or not.

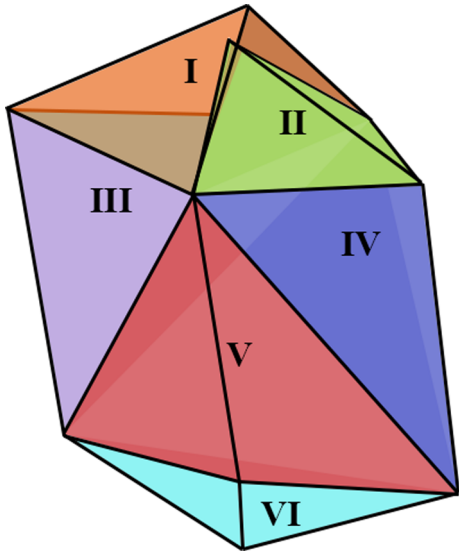


Fig. 4. Scenarios of overlap detection for tetrahedrons in extension: (1) overlap (I-II); (2) touch (touch in a facet I-III; a line I-IV; a point I-V); (3) separation (I-VI).

Step (1) - Choosing a triangular facet (ABD).
Step (2) - Generating the minimal circumcircle of ABD and calculating its centroid (C_f) and radius (R_f).
Step (3) - Generating the minimal circumscribed hemisphere of ABD with C_f and R_f.
Step (4) - Randomly picking a point F as the new vertex inside the hemisphere, refer to formulae (3–5).
Step (5) - Checking whether F fulfills the requirements (e.g. convexity, no overlap, and extension degree) or not. If it does, go to step (6); otherwise, update the retry number ($r = r + 1$) and return to step (4).
Step (6) - Adding F to the current polyhedron, and updating vertices, edges, facets, and the number of current iteration ($i = i + 1$).

$$x_f = \frac{x_a + x_b + x_d}{3} + R_f \times ran_0 \times cos(360^\circ \times ran_1) \times sin(180^\circ \times ran_2) \tag{3}$$

$$y_f = \frac{y_a + y_b + y_d}{3} + R_f \times ran_0 \times sin(360^\circ \times ran_1) \times sin(180^\circ \times ran_2) \tag{4}$$

$$z_f = \frac{z_a + z_b + z_d}{3} + R_f \times ran_0 \times cos(180^\circ \times ran_2) \tag{5}$$

where, $F(x_f, y_f, z_f)$ is the new vertex; $A(x_a, y_a, z_a)$, $B(x_b, y_b, z_b)$ and $D(x_d, y_d, z_d)$ are the vertices of triangular basic facet; ran_0, ran_1, and ran_2 are three random factors within a prescribed range (e.g., from 0 to 1).

2.2.3. Extension process control

Sections 2.2.1 and 2.2.2 introduce the procedures of each iteration in REM and PEM, respectively. The methods to control the entire extension process are given below.

In both REM and PEM, the basic facets were chosen according to the radius lengths of their minimal circumcircles. Usually, the longest

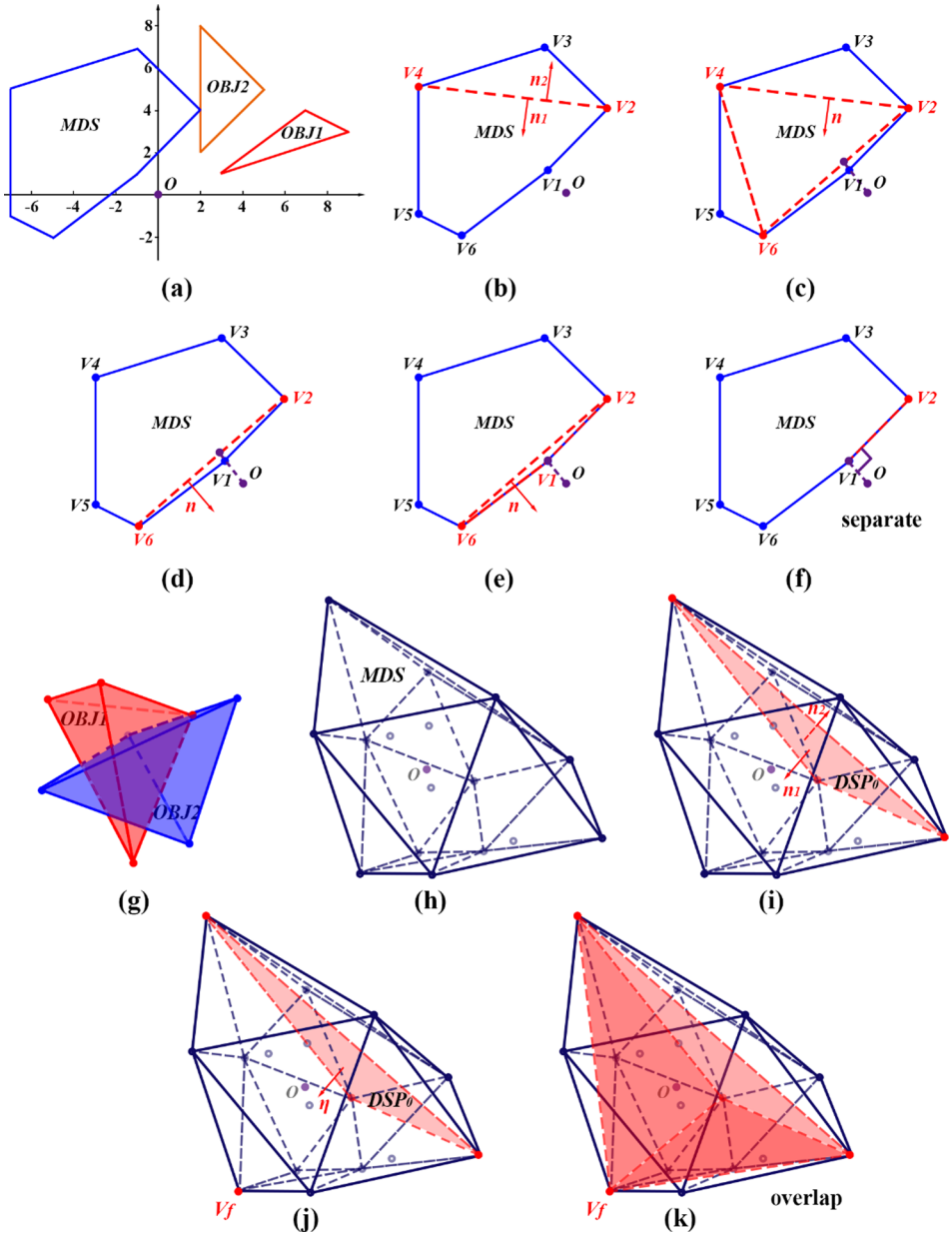


Fig. 5. Schematic illustration of the enhanced GJK overlap detection procedures for: (a-f) two separated triangles; and (g-k) two overlapped tetrahedrons.

radius is selected as the criteria for choosing a basic facet for the extension. If the shortest radius or a random radius was selected as the criterion, the newly generated tetrahedrons would congregate at the part that had more small triangular facets (Fig. 2b).

In REM and PEM, once the new vertex was unable to fulfill the requirements, it would be regenerated randomly. As the number of current iteration (i) increased, the computational effort of regenerating vertex increased dramatically. To speed up the convergence of this algorithm, a feedback mechanism was introduced herein. First, an index indicating the extension degree for an iteration was defined. Taking Fig. 1(b) as an example, the extension degree can be written as:

$$E(e) = \frac{h_e}{R_e} \tag{6}$$

where, h_e is the distance from the new vertex to its basic facet; R_e is the radius of the minimal circumcircle of the basic facet (BCD). The extension degree index, $E(e)$, has a positive correlation with angularity and a negative correlation with roundness (Barrett, 1980). To speed up the convergence, $E(e)$ should decrease with the increase of the current vertices number (i) and retry number (r) for regeneration, which can be controlled by a user-customized function, $F(i, r)$.

2.3. Convexity control

If a polyhedron was on the same side of the planes defined by each of its facets, the polyhedron would be a convex polyhedron. Sometimes polyhedron convexity is required, which raised the problem of convexity control. In the original REM (Guo et al., 2017), convexity control was not mentioned. Compared with REM, the oriented volume method in PEM (Du et al., 2013) can ensure that the new vertex is generated in the outward hemisphere as depicted by Fig. 1(c). However, the PEM still cannot provide strict convexity as defined. In light of this, a two-step method was proposed herein to ensure the convexity of polyhedrons in case the convexity was required.

The first step was to ensure that the generated point was outside the existing part of the polyhedron. This could be achieved by checking whether the newly generated point $V_i(x_i, y_i, z_i)$ and the origin (O) were on different sides of the basic facet (LMN) plane or not (Fig. 3a-b).

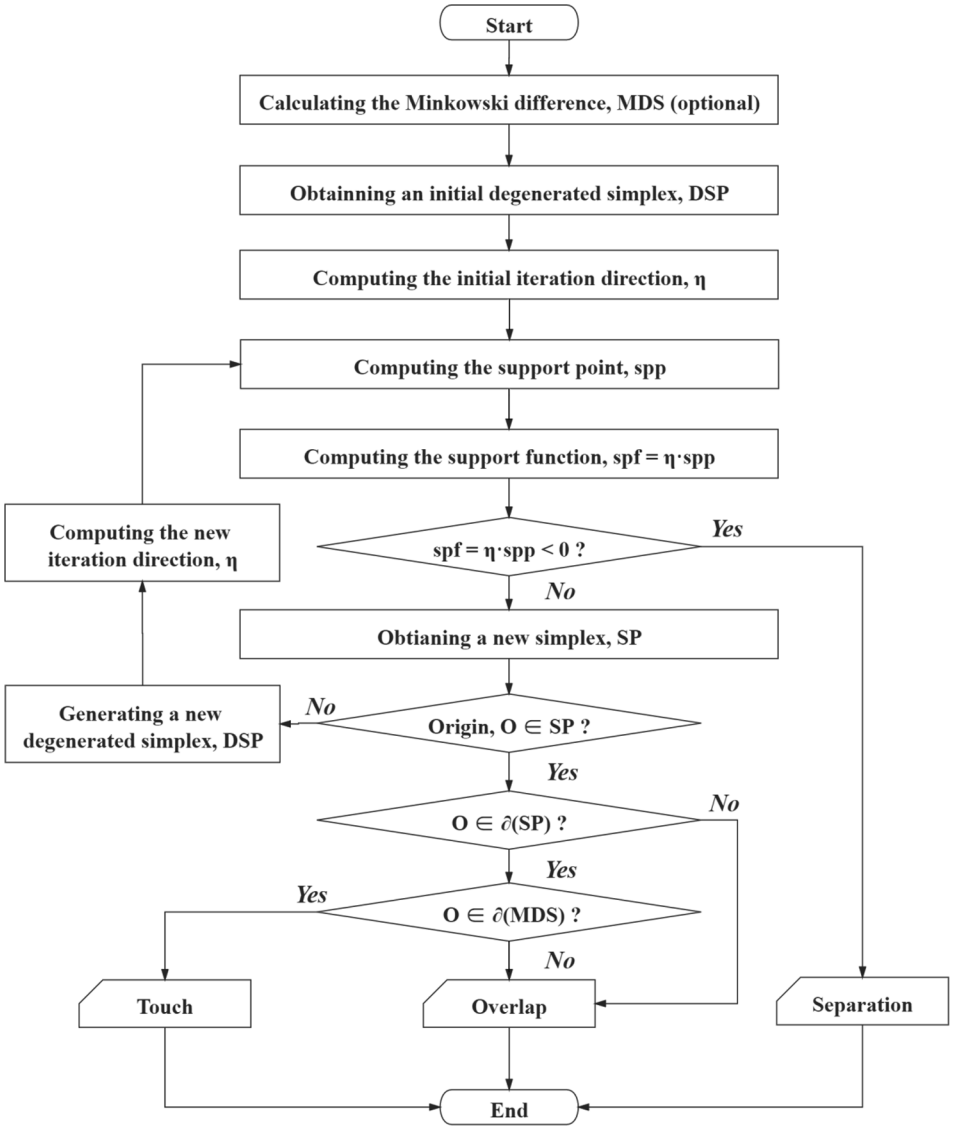


Fig. 6. Flow chart for the enhanced GJK overlap detection algorithm.

Supposing the expression of the facet (LMN) is:

$$a_i x + b_i y + c_i z + d_i = 0 \tag{7}$$

Then, the condition in the first step can be written as:

$$sign(d_i \cdot (a_i x_i + b_i y_i + c_i z_i + d_i)) = -1 \tag{8}$$

where $sign(X) = (+1, 0, -1)$ when X is $(> 0, = 0, < 0)$.

The second step was to ensure the convexity of the newly generated polyhedron by checking the definition of a convex polyhedron. In other words, for the plane of each triangular facet of the polyhedron, all the vertices were on the same side of the plane. As shown in Fig. 3(d), the entire polyhedron was encompassed by the corner formed by the 3 planes (LMV_i, MNV_i, and NLV_i). Supposing the 3 planes (LMV_i, MNV_i, and NLV_i) can be expressed as:

$$a_{ij} x + b_{ij} y + c_{ij} z + d_{ij} = 0, \quad j = 1, 2, 3 \tag{9}$$

Then, for any one of the polyhedron vertices $K(x_k, y_k, z_k)$ (e.g., P, Q, L, M, N, V_i in Fig. 3d), this condition can be written as:

$$sign(d_{ij} \cdot (a_{ij} x_k + b_{ij} y_k + c_{ij} z_k + d_{ij})) = 0 \ \ or \ \ 1 \tag{10}$$

where, i indicates vertex V_i; j ($j = 1, 2, 3$) indicates the 3 new facets (LMV_i, MNV_i, and NLV_i); and k indicates all vertices in the polyhedron (e.g., P, Q, L, M, N, V_i in Fig. 3d).

In this method, for each loop in the iteration process, only 3 newly generated facets instead of all facets would be checked, which reduced the computational effort significantly. Since the convexity was checked in each iteration by this two-step method, the whole process could ensure the convexity of the final polyhedron.

It should be pointed out that overlap detection is not required in this two-step method. Because the new vertex is always generated on the base of a convex polyhedron as well as the new vertex and the existing convex polyhedron are on different sides of the basic facet, they are unable to overlap with each other.

2.4. Overlap detection by the GJK algorithm

Because one tetrahedron may overlap with another in extension, overlap detection is essential for the extension method. The original REM (Guo et al., 2017) did not pay attention to the problem of overlap detection. In the original PEM (Du et al., 2013), overlap detection was achieved by comparing $\sum V_V$ and V_Ω.; however, it was unable to be applied to some special cases (e.g., a newly generated vertex is not inside a tetrahedron of an existing polyhedron, but overlap does happen). By decomposing the entire polyhedron into tetrahedrons, the enhanced GJK algorithm can be applied for overlap detections for

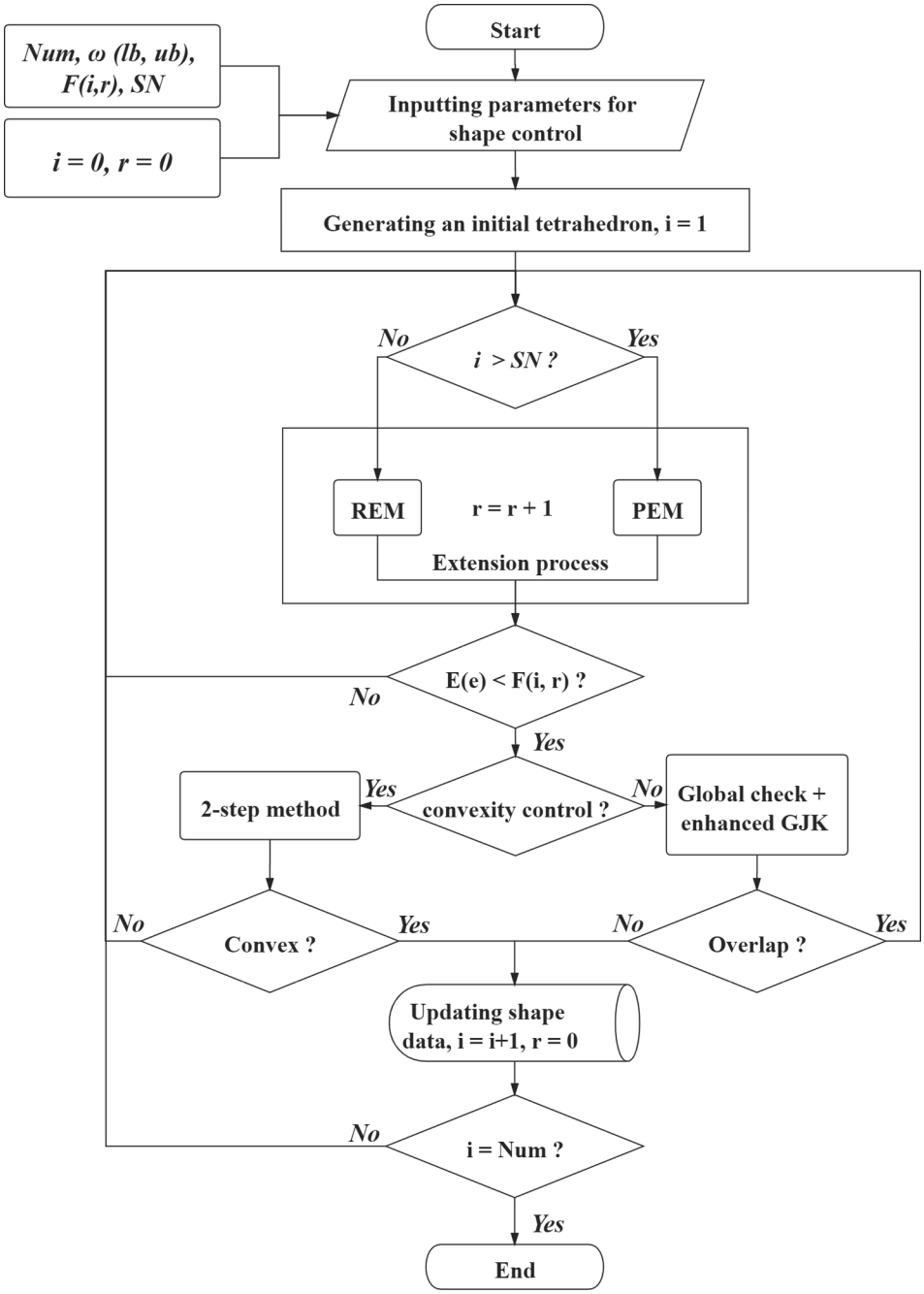


Fig. 7. Flow chart for the proposed hybrid extension method (HEM).

polyhedrons.

2.4.1. Brief introduction of the GJK algorithm

The GJK algorithm (Gilbert et al., 1988) and its variants (Cameron, 1997; Van De Bergen, 1999) can compute the closest Euclidean distance or the penetration depth of two convex objects. In this study, only the contact state (separation, touch or overlap) of two objects is of concern (Fig. 4); hence, the part for calculating the value of distance or depth is not introduced herein. By using the Minkowski difference (Hadwiger, 1950) of two convex objects, overlap detection can be converted to determine the relationship between the origin and the space occupied by the Minkowski difference. It can be achieved by dynamically investigating the relative position between the origin and the simplices inside the Minkowski difference space (Fig. 5).

2.4.2. Preliminaries

For two objects, $OBJ1$ and $OBJ2$, the spaces occupied by them can be marked as SP_A and SP_B, and the boundaries can be denoted by $\partial(SP_A)$ and $\partial(SP_B)$. Their contact state can be expressed mathematically: separation ($SP_A \cap SP_B$); $= \varnothing$), touch ($SP_A \cap SP_B = \partial(SP_A) \cap \partial(SP_B)$), and overlap ($SP_A \cap SP_B \neq \varnothing$) (Feng and Tan, 2019).

2.4.2.1. Minimum translational distance (MTD). The minimum translational distance (MTD) indicates the shortest distance it will take to make the two objects ($OBJ1$ and $OBJ2$) into a touch state, which can be denoted by $MTD(SP_A, SP_B)$. It should be pointed out that $MTD(SP_A, SP_B)$ features a negative sign when $OBJ1$ and $OBJ2$ overlap with each other. The contact state ($CS(OBJ1, OBJ2)$) can be written as:

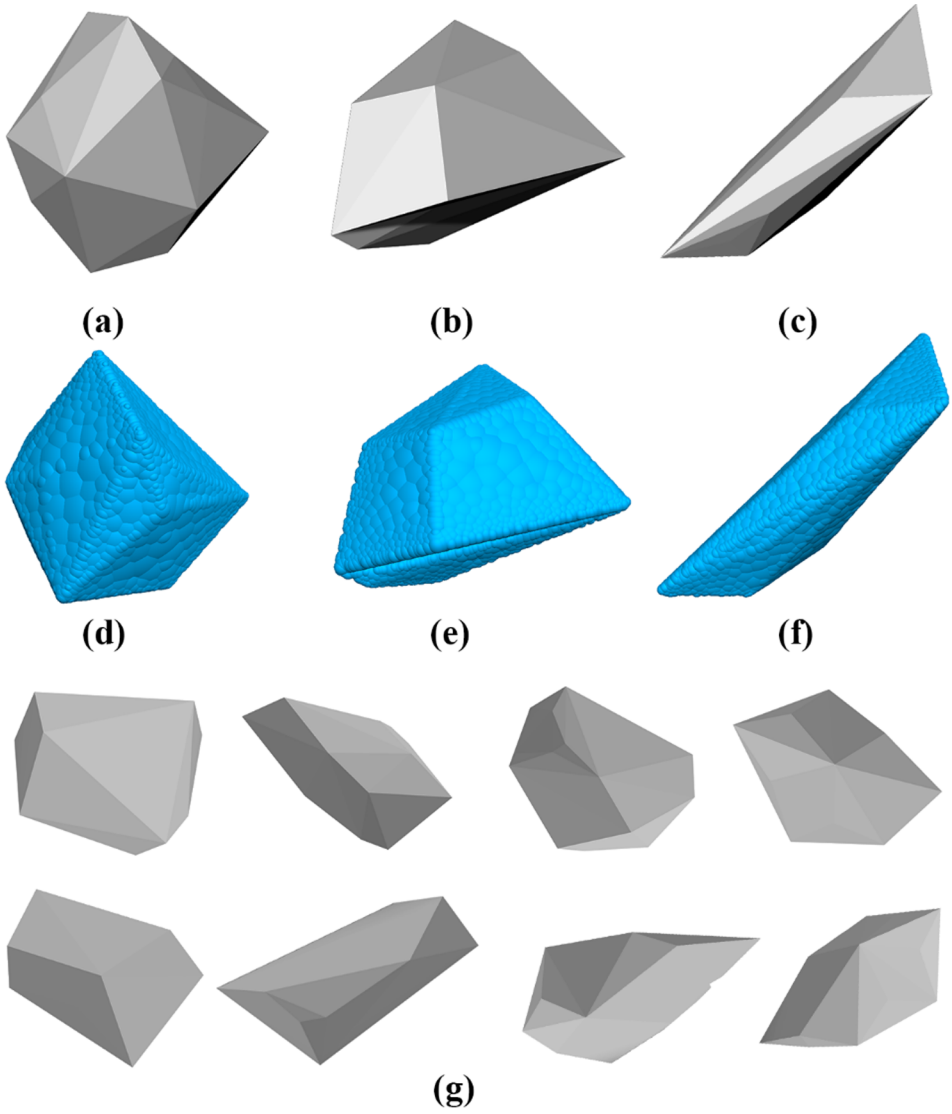


Fig. 8. Polyhedrons generated by HEM: (a) an equant polyhedron; (b) a platy polyhedron; (c) an elongated polyhedron; (d-f) reconstruction of polyhedrons in DEM by the bubble pack algorithm; and (g) other various polyhedrons.

Table 1
Polyhedrons Generated by HEM.

Polyhedron	Form	Convexity	***Num***	***SN***	[***lb***, ***ub***]	Elapsed time
1	Compact	Convex	18	10	[0.12, 0.1225]	0.380 s
2	Platy	Concave	15	10	[0.09, 0.10]	0.290 s
3	Elongated	Convex	18	10	[0.02, 0.03]	0.221 s

$$CS(OBJ1,\ OBJ2) = sign(MTD(SP_A,\ SP_B)) = \begin{cases} 1,\ separation \\ 0,\ touch \\ -1,\ overlap \end{cases} \tag{11}$$

As implied by formula (11), the sign of *MTD* can be used to distinguish different contact states. In HEM, for the extending iteration, the separation state ($CS = 1$, scenario I-VI in Fig. 4) and the touch state ($CS = 0$, scenarios I-III, I-IV, and I-V in Fig. 4) are acceptable; while, the overlap state ($CS = -1$, scenario I-VI in Fig. 4) is unacceptable.

2.4.2.2. Minkowski difference. For two sets SP_A, $SP_B \subset R^3$, the Minkowski sum or difference can be expressed as:

$$SP_A \pm SP_B = \{x_A \pm x_B\colon x_A \in SP_A,\ x_B \in SP_B\} \tag{12}$$

If the two objects to be investigated are convex, their Minkowski difference is convex as well. Moreover, every vertex on the convex hull of the Minkowski difference is derived from two boundary vertices, one from SP_A and the other from SP_B. The space occupied by the Minkowski difference can be denoted by formula (13) (Fig. 5a and h).

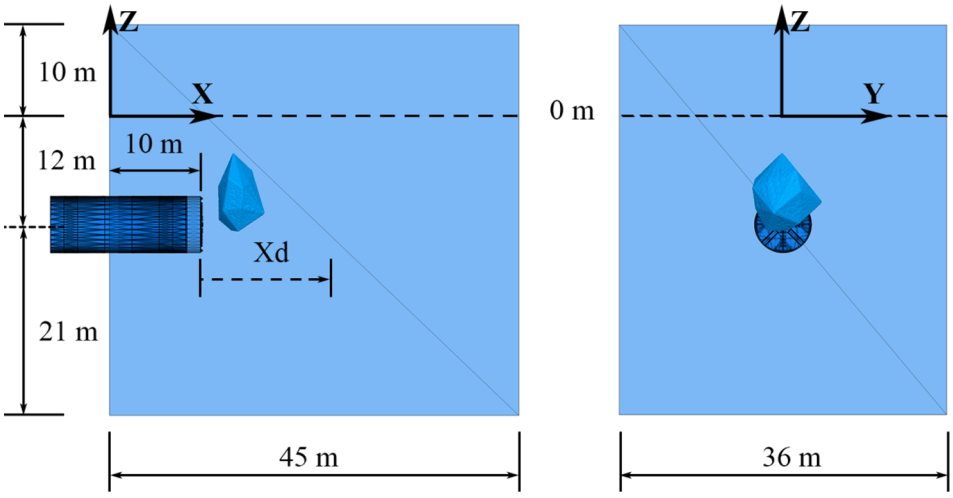
$$MDS(SP_A,\ SP_B) = \{x_A - x_B\colon x_A \in SP_A,\ x_B \in SP_B\} \tag{13}$$

If $OBJ1$ and $OBJ2$ overlap with each other, there exists at least one point, x_{AB}, contained by these two objects simultaneously. Thus, $x_{AB} - x_{AB} \in MDS(SP_A,\ SP_B)$, i.e. the origin, $O \in MDS(SP_A,\ SP_B)$. Similarly, if the two objects are separated, $O \notin MDS(SP_A,\ SP_B)$. If they are in a touch state, $O \in \partial(MDS(SP_A,\ SP_B))$, where $\partial(MDS(SP_A,\ SP_B))$ stands for the boundary of the *MDS*. Therefore, investigating the relative position between two objects is converted to investigating the relative position between the origin and the Minkowski difference of the two objects (formula 14).

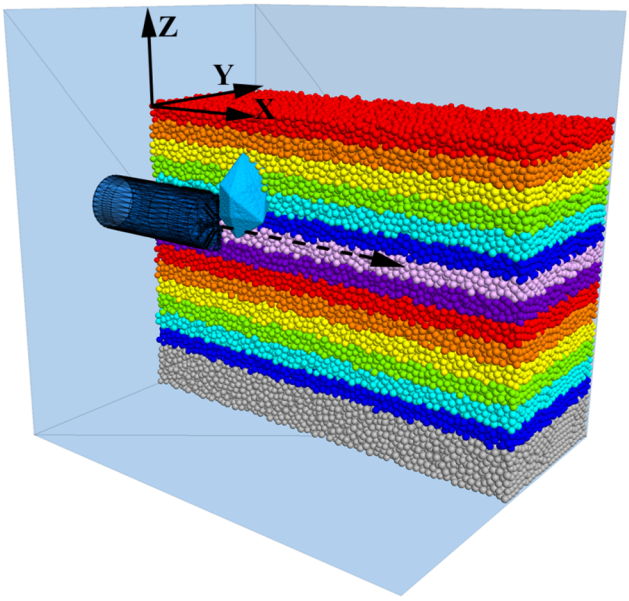
$$MTD(SP_A,\ SP_B) = MTD(O,\ MDS(SP_A,\ SP_B)) = MTD(O,\ SP_A - SP_B) \tag{14}$$

Furthermore, formula (11) can be rewritten as:

$$CS(OBJ1,\ OBJ2) = sign(MTD(SP_A,\ SP_B)) = sign(MTD(O,\ SP_A - SP_B)) \tag{15}$$



(a) side and front views of the model



(b) 3D view of the model

Fig. 9. Schematic illustration of the DEM model by its: (a) side and front views; and (b) 3D view.

2.4.2.3. Simplex. Simplex (e.g., a dot, line segment, triangle, and tetrahedron) is the most basic unit in topology. For the GJK algorithm and its variants, simplex forms in 3D space are triangles and tetrahedrons (Fig. 5i-k). In 3D space, a triangle is viewed as a degenerated simplex form of a tetrahedron. In the GJK algorithm, the simplex shifts dynamically between triangle and tetrahedron for updating.

2.4.2.4. Support function and support point. Based on a given direction, η, the support function, $spf_{DS}(\eta)$, can determine the farthest vertex (V_f) (Fig. 5c, e and j) along η in the domain spaceDS (usually MDS, SP_A, or SP_B).

$$spf_{DS}(\eta) = max\{v \cdot \eta : v \in DS\} \tag{16}$$

If $spp_{DS}(\eta)$ is used to denote the solution of formula (16) (V_f), it can be expressed as:

$$spf_{DS}(\eta) = spp_{DS}(\eta) \cdot \eta,\ spp_{DS}(\eta) \in DS \tag{17}$$

Thereby, $spp_{DS}(\eta)$ can be written as:

$$spp_{DS}(\eta) = \{V_f : \forall\, v \in DS,\ V_f \cdot \eta \geq v \cdot \eta,\ V_f \in DS\} \tag{18}$$

$spp_{DS}(\eta)$ is called as the support point. Each point in $MDS(SP_A, SP_B)$ is derived from a pair of points from SP_A and SP_B, respectively. Due to the addictive nature of Minkowski difference, formula (16) can be rewritten as below:

$$spf_{MDS}(\eta) = spf_{SP_A - SP_B}(\eta) = spf_{SP_A}(\eta) + spf_{SP_B}(-\eta) \tag{19}$$

Moreover, the support function can be expressed as:

$$spf_{MDS}(\eta) = spp_{MDS}(\eta) \cdot \eta = spp_{SP_A}(\eta) \cdot \eta - spp_{SP_B}(-\eta) \cdot \eta \tag{20}$$

Then, $spp_{MDS}(\eta)$ can be expressed as:

$$spp_{MDS}(\eta) = spp_{SP_A}(\eta) - spp_{SP_B}(-\eta) \tag{21}$$

where, $spp_{MDS}(\eta)$ is the farthest vertex along the direction of η in MDS; $spp_{SP_A}(\eta)$ and $spp_{SP_B}(-\eta)$ are the farthest points of $SP_A SP$ and $SP_B SP$ along the directions η and $-\eta$, respectively.

It can be deduced from the definitions of the support function and the support point that the support point must be on the convex hull of the domain space, i.e., $\partial(SP_A)$, $\partial(SP_B)$, or $\partial(MDS(SP_A, SP_B))$. Whether

Table 2
Model parameters used in DEM simulation.

Items	Value	Unit
Model Dimensions		
Length	45.00	m
Width	36.00	m
Height	43.00	m
Matrix Dimensions		
Length	45.00	m
Width	36.00	m
Depth	33.00	m
TBM Parameters		
TBM type	EPB	–
Cutter head diameter	6.25	m
Cutting diameter	6.25	m
Shield diameter	6.25	m
Shield length	9.00	m
Chamber length	1.50	m
Aperture rate	42.71	%
Burial depth	12.00	m
Advancing speed	0.02	m/s
Rotational speed	0.1	rad/s

Table 3
Microscopic parameters.

Items	Value	Unit
Soil (Ball)		
Normal stiffness, $\boldsymbol{k_n}$	1×10^8	N/m
Tangential stiffness, $\boldsymbol{k_s}$	5×10^7	N/m
Friction coefficient, $\boldsymbol{\mu}$	0.50	–
Radius	0.25–0.30	m
Boulder (Clump)		
Normal stiffness, $\boldsymbol{k_n}$	1×10^9	N/m
Tangential stiffness, $\boldsymbol{k_s}$	5×10^8	N/m
Friction coefficient, $\boldsymbol{\mu}$	0.5	–
Size	4 or 6	m
TBM (Wall)		
Normal stiffness, $\boldsymbol{k_n}$	1×10^{10}	N/m
Tangential stiffness, $\boldsymbol{k_s}$	5×10^9	N/m
Friction coefficient, $\boldsymbol{\mu}$	0.5	–
Boundaries (Wall)		
Normal stiffness, $\boldsymbol{k_n}$	1×10^9	N/m
Tangential stiffness, $\boldsymbol{k_s}$	5×10^8	N/m
Friction coefficient, $\boldsymbol{\mu}$	0	–

two objects are separated or not can be checked by judging whether the value of the support function is smaller than zero or not, i.e.,

$$spf_{MDS}(\eta) = spp_{MDS}(\eta)\cdot\eta = spp_{SP_A}(\eta)\cdot\eta - spp_{SP_B}(-\eta)\cdot\eta < 0 \quad (22)$$

2.4.3. Procedures of GJK overlap detection

2.4.3.1. Procedure outline. I– Initialization

1. Calculating the *MDS* of two given objects, *OBJ*1 and *OBJ*2 (optional) (Fig. 5a and h).
2. Generating 3 non-collinear vertices on the boundary of the *MDS* to form an initially degenerated simplex, DSP_0 (Fig. 5b and i).
3. Obtaining the normal vector of the triangular facet as the initial iteration direction, η_0, which directs to the side containing the origin (Fig. 5b-c and i-j). If the origin locates in the plane that contains the DSP_0, either of the two normals can be chosen as η_0.

II – Iteration

1. Obtaining the support point $spp_{MDS}(\eta)(V_f$, refer to Fig. 5c and j).
2. Calculating the support function, $spf_{MDS}(\eta) = spp_{MDS}(\eta)\cdot\eta$. If $spf_{MDS}(\eta) < 0$, the contact state, return$CS = 1$ (SEPARATION).
3. Updating the Simplex, *SP*
   a. Obtaining a new tetrahedral simplex, *SP*, by combining the support point, $spp_{MDS}(\eta)$, and degenerating simplex, *DSP*, as a new tetrahedron.
   b. Checking whether *SP* encloses the origin or not. If not, go to II.3.c; if yes, go to step i below:
      i. Checking whether the origin is on the surface of *SP* or not. If not, return $CS = -1$(OVERLAP); if yes, go to step ii below:
      ii. Checking whether the origin is on the convex hull of *MDS* or not. If yes, return $CS = 0$ (TOUCH); if not, return $CS = -1$ (OVERLAP).
   c. By discarding a vertex, the simplex, *SP*, can be reduced to a new degenerated simplex, *DSP* (*DSP* is a triangular facet that contains the closest point to the origin) (Fig. 5c).
   d. *DSP* has two normal vectors and one of them directs to the origin. Taking this normal vector as the new iteration direction, η, and going to II. 1 (Fig. 5d).

2.4.3.2. Procedure details.

The aim of initialization in procedure I is to generate an initial degenerated simplex that contains 3 non-collinear vertices from the boundary of *MDS*. A larger triangular facet usually means a faster algorithm convergence. Moreover, explicit computation of the *MDS* can provide an intuitive idea of the whole procedure; however, it will increase the computation effort. This explains why it is marked as an optional procedure (Fig. 6).

If there is no vertex on the boundary of the *MDS* further than the origin along the current iteration direction, the two objects investigated can be determined as separated, refer to Fig. 5f. Moreover, once the separation state is determined, the minimal distance between the two objects can be determined, which is equal to the distance between the origin and the current triangular facet, *DSP*. For the current simplex, the check of the enclosure of the origin (Section 2.4.3.1) can refer to formula (1).

Given that the polyhedrons are extended by adding new tetrahedrons, the preceding procedures of the enhanced GJK overlap detection can be applied for the current tetrahedron and the existing ones. To reduce the computational effort, global detection will be used before local detection. Global detection uses a simple enclosure of the object for executing a rough and effective check, e.g., the bounding box. For two objects whose bounding boxes overlap with each other, local detection (e.g. the GJK algorithm) can be used for further overlap detection. By decomposing the whole polyhedron into tetrahedrons, GJK overlap detection can be applied for the generation of polyhedrons with various shapes, not only convex ones.

2.5. Hybrid extension method

Based on the improved REM and PEM introduced previously, a hybrid extension method (HEM) was proposed herein. In HEM, the polyhedron can be firstly extended by the improved REM, and then extended by the improved PEM for overcoming the disadvantages of REM and PEM. As shown in Fig. 7, the HEM can be outlined as:

Step (1) - Inputting shape control parameters, e.g., number of vertices (*Num*), volume ratio (ω), extension degree control function ($F(i, r)$), turning point of REM and PEM (*SN*).
Step (2) - Generating an initial tetrahedron and setting $i = 1$.
Step (3) - Checking whether $i > SN$. If not, go to step (4); otherwise, go to step (5).
Step (4) - Extending the polyhedron by the improved REM and setting $r = r + 1$.
Step (5) - Extending the polyhedron by the improved PEM and setting $r = r + 1$.
Step (6) - Checking whether $E(e) < F(i, r)$ or not. If yes, go to step (7); otherwise, go back to step (3).
Step (7) - Checking whether the convexity is required or not. If yes, go to step (8); otherwise, go to step (9).

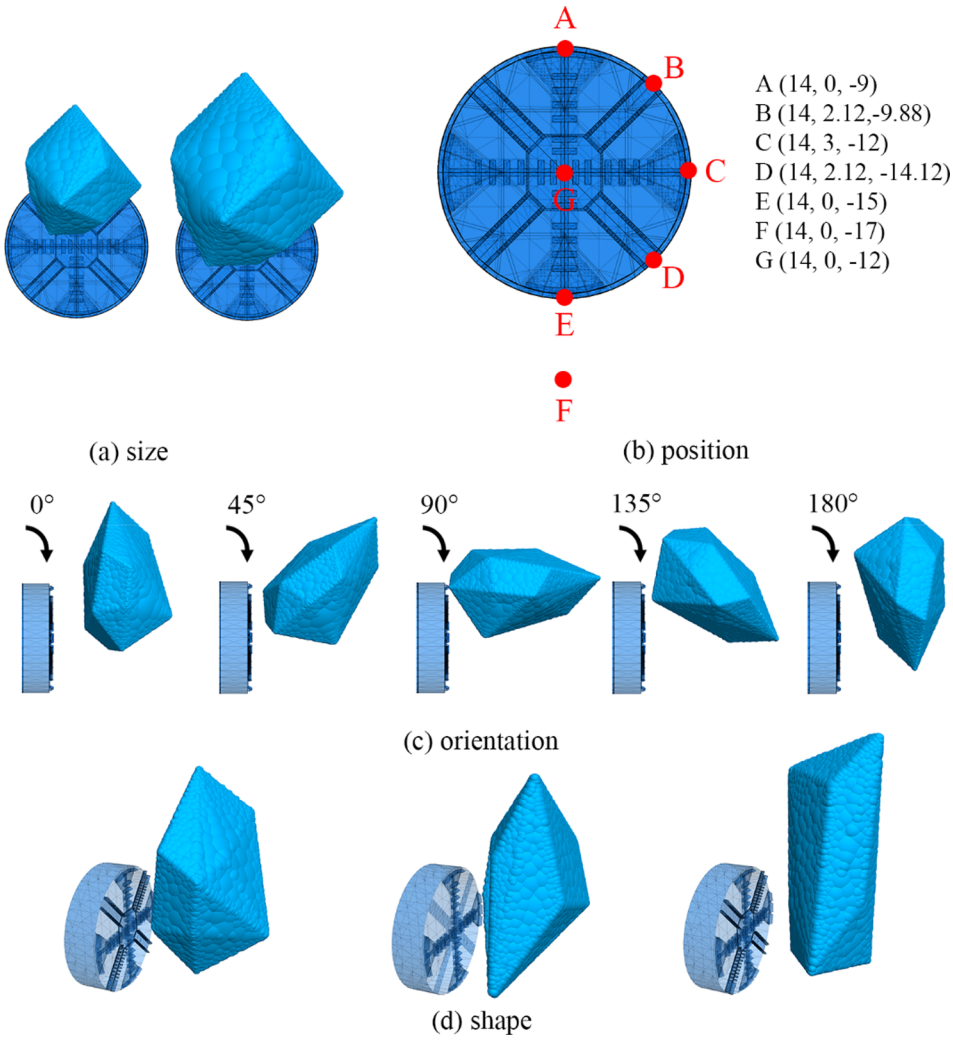


Fig. 10. Schematic illustration of the orthogonal tests for exploring the influence of: (a) boulder size, (b) boulder position, (c) boulder orientation, and (d) boulder shape.

Step (8) - Checking whether the polyhedron is convex or not by the two-step convexity control method. If yes, go to step (10); otherwise, go back to step (3).
Step (9) - Checking whether there is overlap or not by global detection (e.g. bounding box) first and then by the enhanced GJK algorithm. If not, go to step (10); if yes, go back to step (3).
Step (10) - Updating the data (vertices, edges, facets, and etc.), setting $i = i + 1$, $r = 0$, and then going to step (11).
Step (11) - Checking whether the current vertex number is enough or not. If yes, end; otherwise, go back to step (3).

2.6. Applications of the HEM

Three polyhedrons (an equant one, a platy one, and an elongated one) were generated and selected herein as the applications of the proposed algorithm and the study objects in DEM simulation. The algorithm was coded and run in MATLAB (version R2019b) on a laptop (Lenovo Thinkpad T470p CPU @2.80 GHz RAM 8.00 GB).

As shown in Fig. 8, polyhedron 1 is compact, polyhedron 2 is platy and polyhedron 3 is elongated (Fig. 8a-c). Other information (form, *Num*, SN, [*lb*, *ub*] , and elapsed time) about these 3 polyhedrons has been summarized in Table 1.

3. Simulation of tunneling in boulder-soil matrix

As pointed out by Hunt (2017), the presence of boulders would complicate the TBM tunneling process and even incur damages to TBM or even incidents. In southern and southwestern China, e.g., Guang Zhou, Shen Zhen, Fu Zhou, and Chengdu, where boulders have been frequently encountered in tunneling, improper treatments of boulder often led to geologic hazards, e.g., excessive ground subsidence, significant ground heave, or sinkhole (Lu et al., 2019). If the boulder could be detected in advance, it can be removed or blasted before tunneling or fixed in strata by grouting and then shattered by a shield machine. Unfortunately, an isolated buried boulder would be difficult to be detected in practice by current field exploration and geophysical methods. Without a timely monitoring system, an isolated boulder could remain undetected until it was pushed for some distance by a TBM. This would be very likely to cause a conspicuous ground movement and then damage pre-existing structures or facilities within the affected zone. To reasonably simulate this scenario and explore the associated ground movement mechanism, the proposed algorithm was incorporated into the commercial DEM software PFC3D (Itasca Consultant Group, 2015) for simulating the case, in which an undetected isolated boulder was assumed to be encountered by an advancing TBM.

Table 4
Summary of the designed orthogonal tests.

Test ID	Size (m)	Position	Orientation	Form
1	6	A	I	Compact
2	4	A	I	Compact
3	6	B	I	Compact
4	6	C	I	Compact
5	6	D	I	Compact
6	6	E	I	Compact
7	6	F	I	Compact
8	6	G	I	Compact
9	6	A	II	Compact
10	6	A	III	Compact
11	6	A	IV	Compact
12	6	A	V	Compact
13	6	A	I	Platy
14	6	A	I	Elongated

Note:
(1) Boulder size was marked by the diameter of the sphere whose volume was equal to that of the boulder.
(2) Boulder position was marked by the coordinate of the boulder centroid: A (14, 0, −9); B (14, 2.12, −9.88); C (14, 3, −12); D (14, 2.12, −14.12); E (14, 0, −15); F (14, 0, −17); G (14, 0, −12).
(3) Boulder orientation was marked by the angle that a boulder rotated from its initial orientation in plane Z-X: I, 0°; II, 45°; III, 90°; IV, 135°; V, 180°.
(4) Boulder form indicated one of the shapes listed in Section 2.6 and Fig. 8(a-c).

3.1. Model configurations

3.1.1. Model dimensions

Considering the computational effort and simulation accuracy, the numerical model was 45 m long, 36 m wide and 43 m high (33 m below the ground level and 10 m above the ground level), as described in Fig. 9 and Table 2. To reduce the boundary effect, the distances from TBM shell to both sides of the bounding box were set as 15 m, which was about 2.5 times the TBM diameter. Meanwhile, the distance from the bottom of the TBM shell to the bottom of the bounding box was set to 18 m, about 3 times the TBM diameter.

3.1.2. TBM

In strata containing boulders or rocks, earth pressure balanced (EPB) TBM with an appropriate aperture rate may be the most favorite choice for tunnelling. To reasonably simulate the tunnelling process, a simplified EPB TBM including a cutterhead and a chamber was built up by using rigid wall facets in this DEM model, which allowed the model to simulate the interaction between the cutterhead and matrix (Fig. 9). Meanwhile, the aperture on the cutterhead allowed the model to simulate the interaction of the soil inside and outside the chamber.

To reasonably simulate realistic situations and reduce the boundary effect, the burial depth of the TBM center was set to 12 m and the initial position of the TBM cutterhead was set at 10 m from the left boundary of the soil matrix (Fig. 9a). The TBM used in this simulation was 6.25 m in diameter and 9 m in length, behind which was a 15 m long lining modeled by walls (Table 2 and Fig. 9). Additionally, the TBM in the simulation had a 1.5 m-long chamber to hold soils for balancing the pressure of the excavation face. The cutterhead was equipped with simplified cutters for simulating the disturbance to soils (Wang et al., 2019b). The excavation process was simulated by dividing the region into many segments that were excavated in sequence. Hence, the mucking system was not built up herein.

3.1.3. Boulder

To simulate the isolated boulder in PFC3D, the generated polyhedrons in HEM were applied to serve as the template for generating clumps (boulders in Fig. 8a-c). Then, by incorporating the bubble pack algorithm (Taghavi, 2011) into PFC3D, the boulders were reconstructed by assembling spheres of different radii (Fig. 8d-f). The HEM is designed to generate irregularly shaped polyhedrons, which provides a wide variety of random shapes representing various granular materials (e.g. boulders and gravels). Additionally, using the bubble pack algorithm, the roundness of boulder can be freely controlled. By controlling the radius ratio of the minimal and the maximal spheres in an assembly, users are able to simulate both sharp and blunt edges of boulder. Thus, the HEM can generate the form of a boulder, and the bubble pack algorithm in PFC can be used to control the roundness of the boulder edges, which ensure the adequacy of this approach for simulating boulders or other granular materials.

3.1.4. Soil matrix

To balance the computational efficiency and accuracy, the soil matrix was simulated by spheres whose radii ranged from 0.25 to 0.30 m (Fig. 9). Moreover, the simplest contact model in DEM, linear model, was applied for the whole model. Table 3 summarizes the values of the parameters used for simulation.

3.2. Parameters to be investigated

Using the orthogonal experimental method, 14 tests were designed and performed to explore the influence of boulder size, position, orientation, and morphology (Fig. 10 and Table 4).

In this numerical model, boulder size was characterized by the diameter of the sphere whose volume was equal to that of the boulder. By keeping the other factors constant, diameters equal to 4 m and 6 m were selected for exploring the effect of boulder size (Fig. 10a).

To study the influence of the position of boulder relative to TBM, 7 different relative positions (A, B, C, D, E, F, and G in Fig. 10b) of the boulder to TBM were designed. The boulder position was controlled by the coordinates of boulder centroids.

To explore the influence of boulder orientation, 5 different scenarios depicted by Fig. 10c were designed for simulation, in which the other factors were kept constant.

Finally, to study the influence of boulder morphology, 3 different boulder forms (compact, platy, and elongated shown in Fig. 10d) were simulated.

3.3. Simulation procedures

The simulation procedures can be described by the following steps:

Step I - Generating the wall box and the TBM according to their prescribed dimensions and positions.
Step II - Generating the boulder according to its prescribed size, position, orientation, and shape.
Step III - Generating, balancing, and grouping the matrix, see Fig. 9(b).
Step IV - Dividing the zone to be excavated into 30 cylinders and each cylinder was 0.5 m in length and 3.125 m in radius. The first cylinder started from X = 8.5 m.
Step V - Excavating the 30 cylindrical zones in order. To simulate the excavation, the entire TBM kept a translational speed of 0.02 m/s along + X direction and the cutterhead kept a rotational speed of 0.1 rad/s anticlockwise (viewed from the front of TBM).

3.4. Analyses of the simulation results

Fig. 11 presents the movements of the matrix and boulders at different tunnelling stages for 3 typical boulders, i.e., a compact one (Fig. 11a-d), a platy one (Fig. 11e-h) and an elongated one (Fig. 11i-k). Fig. 12 shows the final states of the numerical tests designed in Section 3.2 (Fig. 10), in which the initial boulder positions are outlined in red lines. Fig. 13 shows the side and the top views of the displacement contour maps of the numerical tests. Since the boulders are invisible in

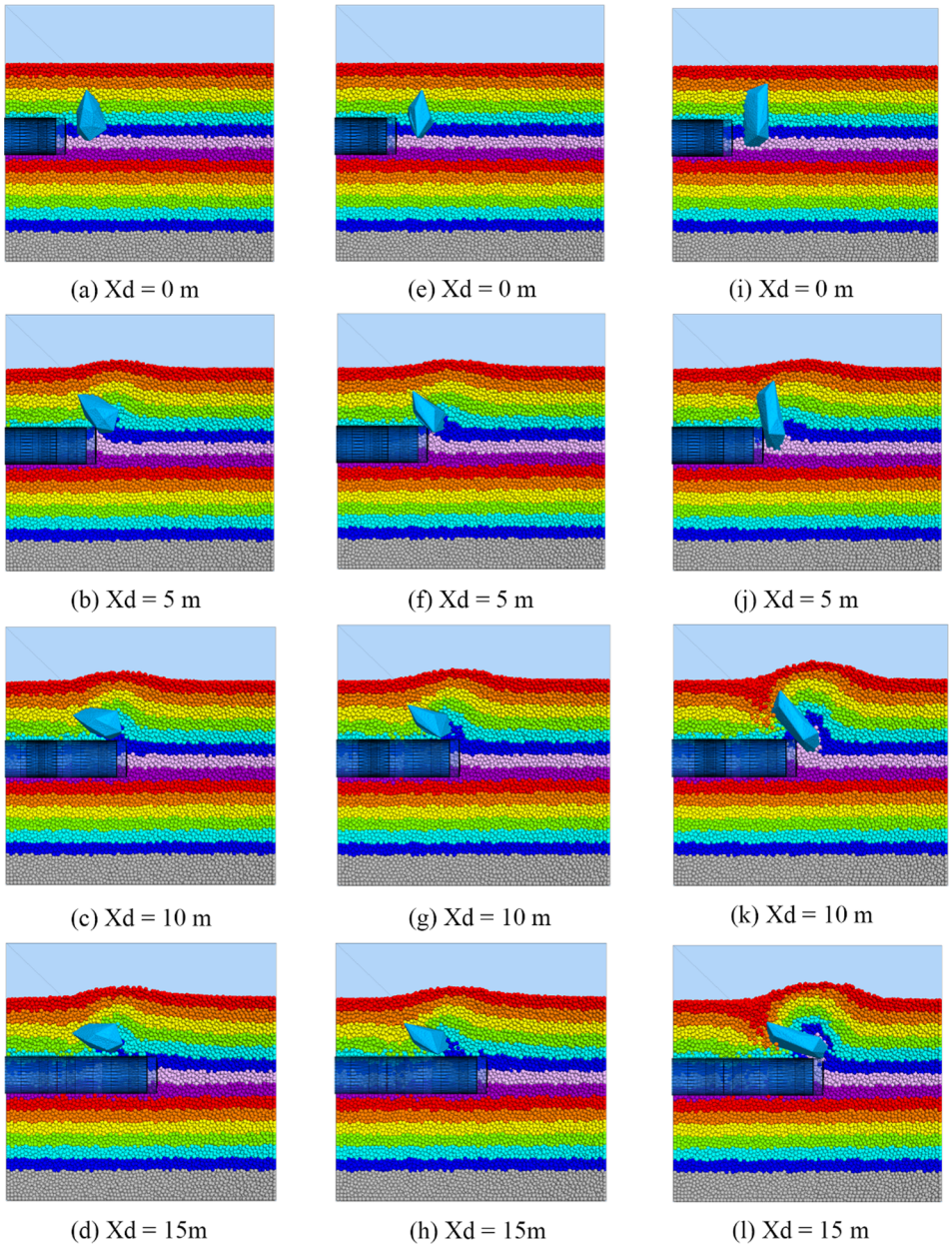


Fig. 11. Schematic illustration of the tunnelling process for 3 typical boulders: (a-d) a compact one; (e-h) a platy one; (i-l) an elongated one.

the case of the top view, they are outlined in red lines for providing better vision. Fig. 14 plots the outlines of ground surfaces corresponding to those numerical tests.

3.4.1. *Influence of boulder size*

The ground heave caused by tunnelling a smaller boulder was apparently smaller than that caused by tunnelling a bigger boulder. Moreover, the area of the ground influence zone for a larger boulder was evidently larger than that for a smaller boulder, refer to Fig. 12a-b, Fig. 13a-b and Fig. 14a. Based upon these results, it can be deduced that if the other factors were kept constant, the larger the boulder size was, the larger the ground influence zone was.

3.4.2. *Influence of boulder position*

As shown by Figs. 12(a, c-h), 13(a, c-h) and 14(a, c-h), boulder position imposed complex influence on the simulation results. Theoretically, it can be assumed that the greater the burial depth of the boulder was, the less the ground surface should be affected. However, the numerical simulation results showed that this assumption is not necessarily true. The results for positions A and F are consistent with the theoretical assumption; while, the results of positions A, E, and G contradicted it, refer to Fig. 14b. This inconsistency was due to that, apart from the burial depth of boulder, the ground influence was also affected by other factors (e.g., the distance a boulder was pushed forward). By comparing the results in Figs. 12, 13 and 14, it can be drawn that the longer the distance a boulder was pushed forward, the greater the ground heave was and the larger the ground influence zone was.

Whether a boulder was pushed aside or ahead by TBM was affected by its distance from the center of TBM cutterhead and its burial depth. When the boulder was near the brim of the cutterhead, such as positions A, B, and C (Fig. 10b), it was very likely to be pushed aside as the TBM advanced. This can be verified by the simulation results plotted in Fig. 12(a, c-d). Although the boulder was near the cutterhead brim for positions D and E (Fig. 10b), it was pushed forward for meters until the end of simulation, refer to Figs. 12(e-f) and 13(e-f). If the boulder centroid was even lower, such as position F in Fig. 10(b), the boulder

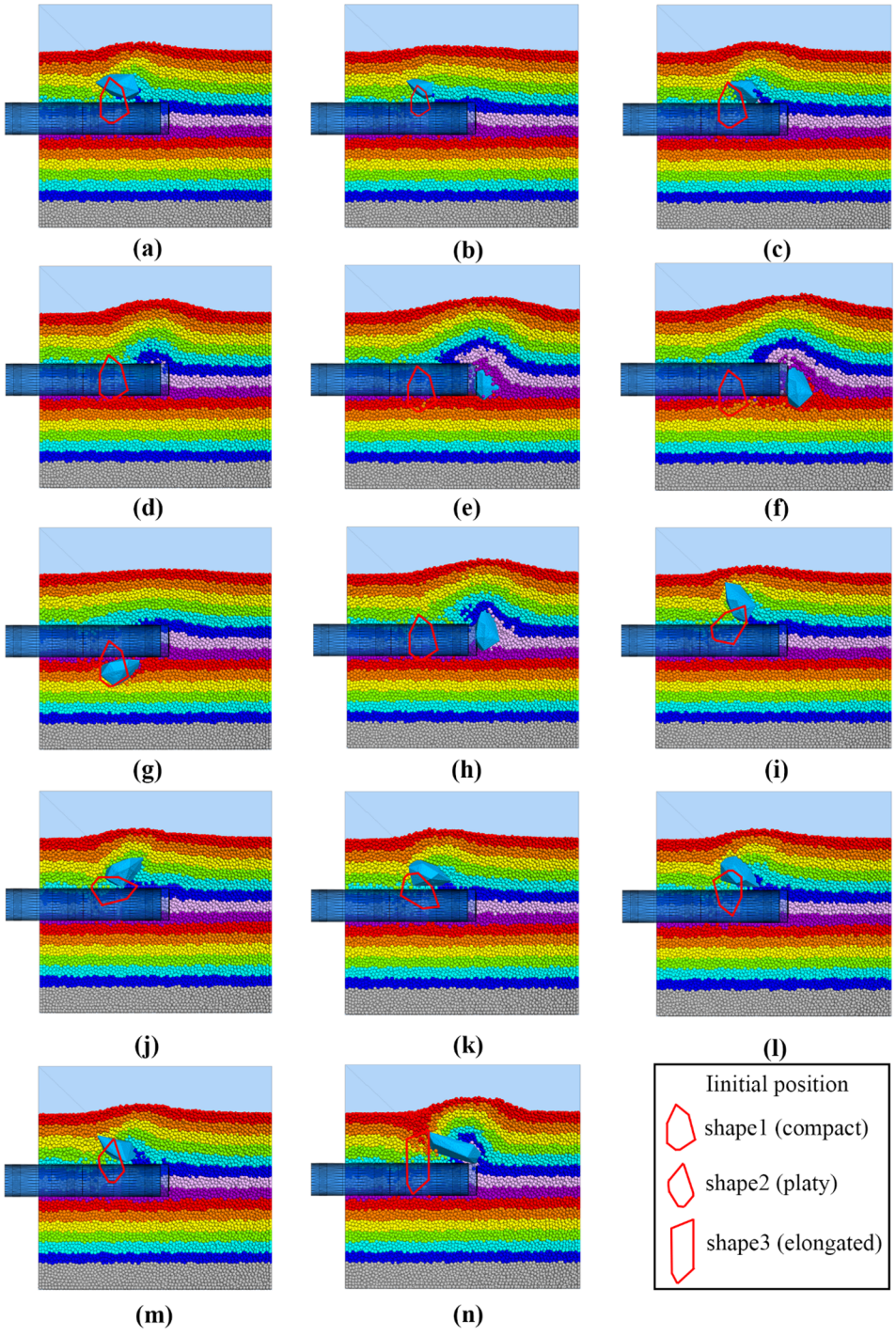


Fig. 12. Schematic illustration of the effects of the initial boulder positions on the simulation results corresponding to the 14 numerical tests in Table 4: (a) Test 1; (b) Test 2; (c) Test 3; (d) Test 4; (e) Test 5; (f) Test 6; (g) Test 7; (h) Test 8; (i) Test 9; (j) Test 10; (k) Test 11; (l) Test 12; (m) Test 13; and (n) Test 14.

would be pushed aside again, refer to Figs. 12g and 13g. These simulation results disclosed that the closer the distance between the boulder centroid and the cutterhead was, the harder the boulder was to be pushed aside. When the boulders were pushed aside, the ground heave heights were generally smaller than the ground heave heights when the boulders were pushed ahead.

The horizontal position of the boulder also had a strong correlation with the horizontal distribution of the ground influence zone. As shown in Figs. 13(c, e) and 14(b), the center of the influence zone on ground surface simultaneously deviated with deviation of the horizontal position of the boulder from the medial. Apparently, this asymmetry was inherently related to the asymmetric horizontal position of the boulder about X axis. Although the boulders in Fig. 13(c and e) shared the same initial horizontal position (B and D in Fig. 10b), the center of influence zone in Fig. 13(e) did not deviate as far as the one in Fig. 13(c) did. This discrepancy was associated with the burial depth of boulder. The influence of boulder horizontal position on the ground surface was partially offset by the effect of boulder burial depth, which in turn verified the aforementioned opinion about the burial depth effect of boulder.

3.4.3. *Influence of boulder orientation*

Figs. 12(a, i-l) and 13(a, i-l) show the influence of boulder

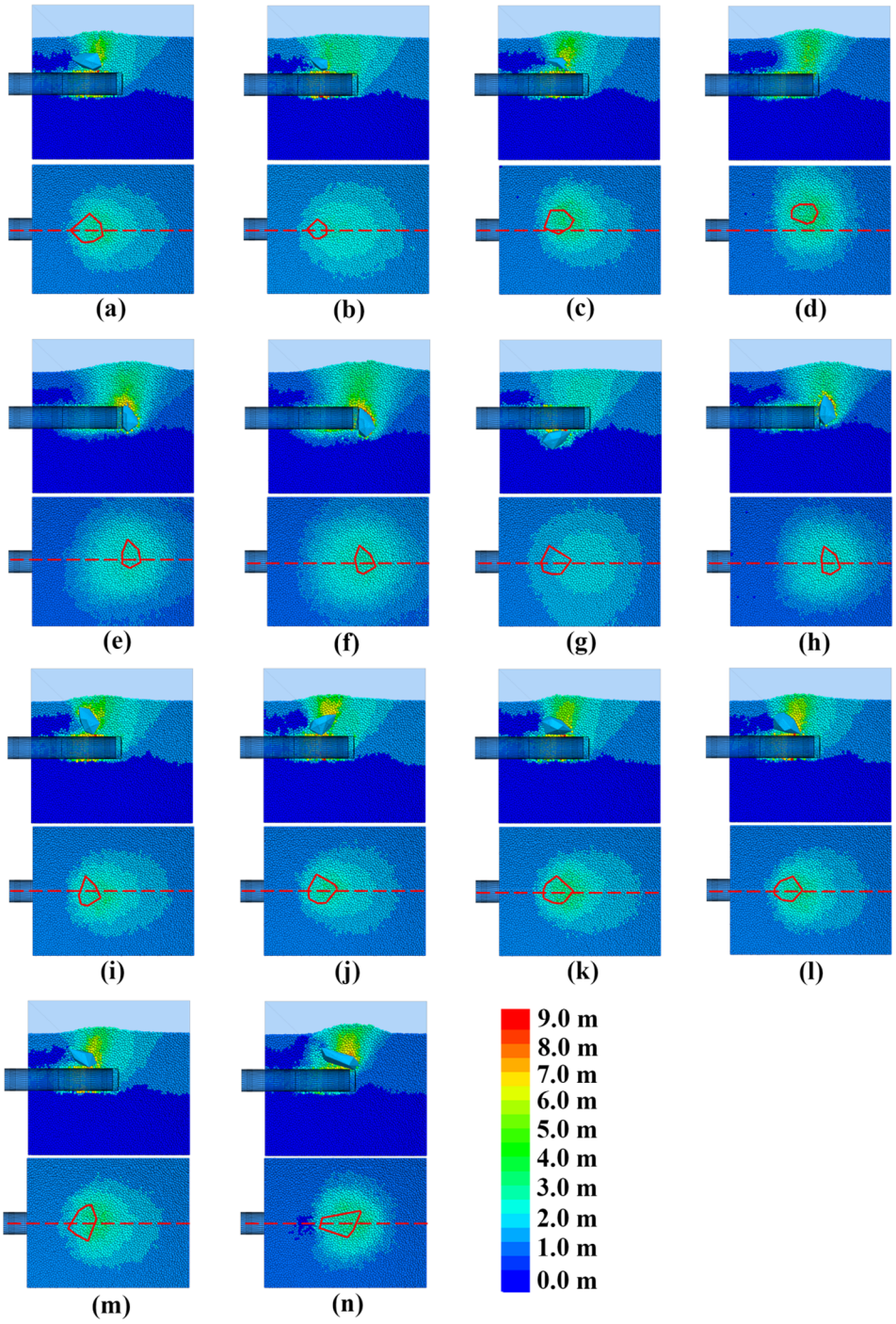


Fig. 13. Side and top views of the matrix displacement contour maps at Xd = 15 m for: (a) Test 1; (b) Test 2; (c) Test 3; (d) Test 4; (e) Test 5; (f) Test 6; (g) Test 7; (h) Test 8; (i) Test 9; (j) Test 10; (k) Test 11; (l) Test 12; (m) Test 13; and (n) Test 14.

orientation. The simulation results show that the boulder orientation rarely affected the size of the ground influence zone (Fig. 14c). The distributions of the ground influence zones for the 5 scenarios are quite similar to each other. However, the trajectories of these 5 boulders were different (Fig. 13), i.e., the boulder trajectory (especially the boulder rotation) was sensitive to the boulder orientation. Consequently, the soil matrix around the boulder was affected by the boulder movement. However, the boulder orientation only locally affected the soil matrix around the boulder.

3.4.4. Influence of boulder morphology

By comparing the numerical test results related to boulder morphology [Figs. 12(a, m, n) and 13(a, m, n)], it can be seen that the size of the ground influence zone was not very sensitive to the boulder shape. In spite of this, there existed some differences associated with boulder shape. For example, all the 3 boulders were pushed aside, but the distances that they were pushed forward were different. Moreover, the shapes of the influence zones on the ground surface were different as well. As ω decreased, the shapes of the influence zone on the ground surface tended to become more oblate.

3.4.5. Summary of the simulation results

The simulation results above show that if a large isolated boulder was not detected and removed ahead of TBM arrival, it could lead to

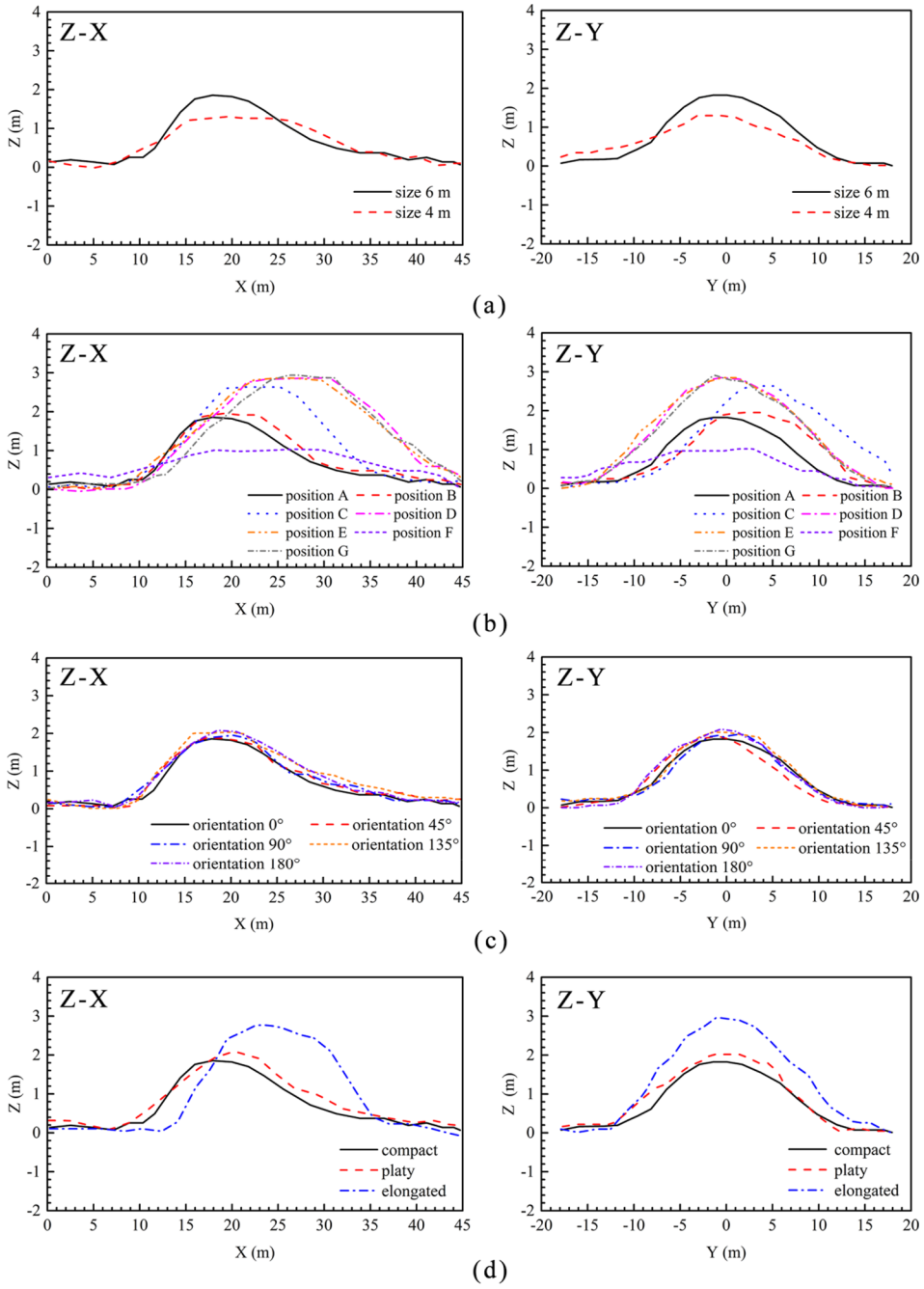


Fig. 14. Ground movements induced by tunnelling in large single boulder-soil matrix with respect to: (a) boulder size; (b) boulder position; (c) boulder orientation; and (d) boulder morphology.

excessive ground heave, in particular at a relatively shallow tunnelling depth. The maximum simulated ground heave due to TBM encountering a large boulder (size = 6 m) was up to 3.0 m and the ground heave widths were approximately 30 m in both the longitudinal and the transversal directions of the tunnelling alignment. The pronounced ground heave could be destructive to pre-existing structures / facilities and pedestrians / vehicles within the affected zone.

4. Conluding remarks

In recent years, isolated boulders in soil matrix have been frequently encountered during tunnelling in Southern and Southwestern China, which incurred both geo-hazards and damages to existing structures and facilities. Because of the discrete nature of boulders, it is extremely difficult for the traditional numerical method (e.g., FEM, FDM and BEM) based on continuum mechanics to investigate the problems involved with boulders or soil-rock mixtures. Due to its 3D irregularly-shaped particle geometry, circular or spherical particles available in the commercial DEM softwares are unable to reasonably simulate boulder particles. To solve this technical difficulty, a systematic approach was proposed in this study for randomly generating polyhedrons for simulation of irregularly shaped particles in DEM. An initial tetrahedron was first created as the basic body by four random points on the unit sphere surface. Then, the initial tetrahedron was extended to the final random polyhedron by HEM, which combines both the improved REM and PEM. To control the extension process, the extension degree can be characterized by an index and controlled by a user-customized function. For generation of convex polyhedrons, a two-step convexity control

method with no need for overlap detection was developed. For cases where polyhedron convexity was not required, the enhanced GJK algorithm was introduced to detect overlaps between the newly generated tetrahedron and the existing ones. By decomposing the entire polyhedron into tetrahedrons, the GJK algorithm can be used to detect overlaps between two arbitrary polyhedrons. All the polyhedron data were generated in MATLAB (Mathworks, 2018) and then imported into PFC3D to generate clump templates for DEM simulations.

To validate the proposed algorithm and explore the influence of the factors of boulder (size, position, orientation, and morphology) on geologic hazards associated with TBM-boulder interaction, extensive numerical simulations were carried out. Based on analyses of the numerical results, the following major conclusions can be obtained:

1. According to the given parameters for shape control, the proposed HEM is able to efficiently generate 3D randomly shaped polyhedrons for simulating granular materials in DEM.
2. The proposed HEM algorithm demonstrated to be an efficient numerical tool for simulation of rocks, boulders, and other granular materials, which can reasonably account for random particle shapes. Because of this merit, it can be incorporated into a 3D commercial DEM software for simulating complex engineering problems in soil-rock mixed strata, e.g., tunneling / excavation in boulder-soil strata or soil-rock mixed strata.
3. If it was not timely detected and then removed, an isolated large boulder encountered by an advancing TBM might result in severe ground heave, especially at shallow tunnelling depth. This would be destructive to pre-existing structures, facilities, pedestrians, and vehicles within the affected zone. Considering these potential risks, adequate attention should be paid to tunnelling in boulder-soil matrix.
4. The size of the influence zone and ground heave height due to the interaction between a large isolated boulder and shallowly tunnelling are affected by boulder size and burial depth as well as the distance between the boulder and the cutterhead centroid. The distribution of the influence zone is consistent with the trajectory of the boulder, which varies with the relative position between boulder and TBM. During tunnelling, boulder movement is sensitive to its morphology and initial orientation.

Author contribution

This paper represents a result of collaborative teamwork. Mr. Shuaiwen Cui developed the 3D algorithm for generation of 3D polyhedrons for simulation of rock particles by DEM under the supervision of both Prof. Yong Tan and Prof. Ye Lu. Mr. Shuaiwen Cui prepared the original manuscript and Prof. Yong Tan and Prof. Ye Lu gave the detailed edit for the original submission. Mr. Shuaiwen Cui performed the additional numerical parametric studies and prepared the revised manuscript under the supervision of Prof. Yong Tan; Prof. Yong Tan and Prof. Ye Lu gave detailed edits for the revised submission.

Declaration of Competing Interest

The authors declare that they have no known competing financial interests or personal relationships that could have appeared to influence the work reported in this paper.

Acknowledgment

Financial support from the National Natural Science Foundation of China (No. 41877286) is gratefully acknowledged. The insightful comments and suggestions from the two anonymous reviewers and Editor-in-Chief Prof. Qianbing Zhang are sincerely appreciated, which have enhanced the presentation of this paper remarkably.

References

Barrett, P.J., 1980. The shape of rock particles, a critical review. Sedimentology 27 (3), 291–303. https://doi.org/10.1111/j.1365-3091.1980.tb01179.x.
Boon, C.W., Houlsby, G.T., Utili, S., 2012. A new algorithm for contact detection between convex polygonal and polyhedral particles in the discrete element method. Comput. Geotech. 44, 73–82. https://doi.org/10.1016/j.compgeo.2012.03.012.
Boon, C.W., Houlsby, G.T., Utili, S., 2015. A new rock slicing method based on linear programming. Comput. Geotech. 65, 12–29. https://doi.org/10.1016/j.compgeo.2014.11.007.
Cameron, S., 1997. Enhancing GJK: Computing minimum and penetration distances between convex polyhedra. In: Proceedings of International Conference on Robotics and Automation, 4 (April), pp. 3112–3117. https://doi.org/10.1109/ROBOT.1997.606761.
Cundall, P.A., 1971. A computer model for simulating progressive large-scale movements in block rock mechanics. Proceedings of the Symposium of International Society of Rock Mechanics.
Cundall, P.A., Strack, O.D.L., 1979. Discrete numerical-model for granular assemblies. Géotechnique 29 (1), 47–65. https://doi.org/10.1680/geot.1979.29.1.47.
Du, C.B., Sun, L.G., Jiang, S.Y., Ying, Z.Q., 2013. Numerical simulation of aggregate shapes of three-dimensional concrete and its applications. J. Aerosp. Eng. 26 (3), 515–527. https://doi.org/10.1061/(ASCE)AS.1943-5525.0000181.
Eliáš, J., 2014. Simulation of railway ballast using crushable polyhedral particles. Powder Technol. 264 (Sep), 458–465. https://doi.org/10.1016/j.powtec.2014.05.052.
Evans, T.M., Chall, S., Zhao, X.L., Rhyne, T.M., 2009. Visualization and analysis of microstructure in three-dimensional discrete numerical models. J. Comput. Civil Eng. 23 (5), 277–287. https://doi.org/10.1061/(ASCE)0887-3801(2009)23:5(277).
Evans, T.M., Frost, J.D., 2010. Multiscale investigation of shear bands in sand: Physical and numerical experiments. Int. J. Numer. Anal. Meth. Geomech. 34 (15), 1634–1650. https://doi.org/10.1002/nag.877.
Ferellec, J.F., McDowell, G.R., 2008. A simple method to create complex particle shapes for DEM. Geomech. Geoeng.: Int. J. 3 (3), 211–216. https://doi.org/10.1080/17486020802253992.
Feng, Y.T., Tan, Y.Q., 2019. On Minkowski difference-based contact detection in discrete/discontinuous modelling of convex polygons/polyhedra: Algorithms and implementation. Eng. Comput. 37 (1), 54–72. https://doi.org/10.1108/EC-03-2019-0124.
Gilbert, E.G., Johnson, D.W., Keerthi, S.S., 1988. A fast procedure for computing the distance between complex objects in three-dimensional space. IEEE J. Robot. Automat. 4 (2), 193–203. https://doi.org/10.1109/56.2083.
Guo, R.Q., Xiao, Y.X., Tang, X.Q., 2017. A fast hybrid realization method for three-dimensional concrete aggregate models. J. Civil Environ. Eng. 39 (5), 100–107 (In Chinese).
Hadwiger, H., 1950. Minkowskische addition und subtraktion beliebiger punktmengen und die theoreme von Erhard Schmidt. Math. Z. 53 (3), 210–218. https://doi.org/10.1007/BF01175656.
Heliot, D., 1988. Generating a blocky rock mass. Int. J. Rock Mech. Mining Sci. Geomech. Abst. 25 (3), 127–138. https://doi.org/10.1016/0148-9062(88)92295-4.
Huang, H., Tutumluer, E., 2013. Image-aided element shape generation method in discrete-element modelling for railroad ballast. J. Mater. Civ. Eng. 26 (3), 527–535. https://doi.org/10.1061/(ASCE)MT.1943-5533.0000839.
Hunt, S.W., 2017. Tunneling in Cobbles and Boulders. Breakthroughs in Tunneling Short Course, Chicago IL, August 14–16.
Jin, L., Zeng, Y. W., Ye, Y., and Xia, L., 2016. Three-dimensional stochastic model of soil-rock mixture based on discrete particle discrete elements and its numerical experiment. J. Yangtze River Sci. Res. Inst., 33(5), 94–101, https://doi.org/10.11988/ckyyb.20150186 (In Chinese).
Lanaro, F., Tolppanen, P., 2002. 3D characterization of coarse aggregates. Eng. Geol. 65 (1), 17–30. https://doi.org/10.1016/S0013-7952(01)00133-8.
Latham, J.P., Munjiza, A., Garcia, X., Xiang, J., Guises, R., 2008. Three-dimensional particle shape acquisition and use of shape library for DEM andFEM/DEM simulation. Miner. Eng. 21 (11), 797–805. https://doi.org/10.1016/j.mineng.2008.05.015.
Lee, Y., Fang, C., Tsou, Y.R., Lu, L.S., Yang, C.T., 2009. A packing algorithm for three-dimensional convex particles. Granular Matter 11 (5), 307–315. https://doi.org/10.1007/s10035-009-0133-7.
Li, Y., Wang, L.B., 2017. Computer-aided procedure for determination of asphalt content in asphalt mixture using discrete element method. Int. J. Pavement Eng. 18 (9), 765–774. https://doi.org/10.1080/10298436.2015.1057140.
Long, M., Menkiti, C., Skipper, J., Brangan, C., Looby, M., 2012. Retaining wall behaviour in Dublin's estuarine deposits. Ireland. Geotech. Eng 165 (6), 351–365.
Lu, Y., Tan, Y., Li, X., Liu, C.N., 2017. Methodology for simulation of irregularly shaped gravel grains and its application to dem modelling. J. Comput. Civil Eng. 31 (5), 04017023. https://doi.org/10.1061/(ASCE)CP.1943-5487.0000676.
Lu, Y., Tan, Y., Li, X., 2018. Stability analyses on slopes of clay-rock mixtures using discrete element method. Eng. Geol. 244, 116–124. https://doi.org/10.1016/j.enggeo.2018.07.021.
Lu, Y., Tan, Y., Chen, W.L., Peng, F.L., Liao, S.M., Song, X.H., Jiang, W.Z., 2019. Numerical study on ground subsidence due to crushing single isolated boulder by tunneling. In: Proceedings of International Conference on Inforatmion Technology in Geo-Engineering, pp. 889–896.
Mathworks, 2018. Matlab r2018a. Natick: The MathWorks, Inc.
Ngo, N.T., Indraratna, B., Rujikiatkamjorn, C., 2014. DEM simulation of the behaviour of geogrid stabilised ballast fouled with coal. Comput. Geotech. 55, 224–231. https://doi.org/10.1016/j.compgeo.2013.09.008.
Itasca Consultant Group, 2015. Particle Flow Code in 3 Dimensions Online Manual

Version 5.0. Consulting Group Incorporated, Minneapolis, Minnesota. Itasca.
Shi, G.H., Goodman, R.E., 1989. The key blocks of unrolled joint traces in developed maps of tunnel walls. Int. J. Numer. Anal. Meth. Geomech. 13 (2), 131–158. https://doi.org/10.1002/nag.1610130203.
Shi, G.H., 1992. Discontinuous deformation analysis: a new numerical model for the statics and dynamics of deformable block structures. Eng. Comput. 9 (2), 157–168. https://doi.org/10.1108/eb023855.
Taghavi, R., 2011. Automatic clump generation based on mid-surface. In: Proceedings, 2nd International FLAC/DEM Symposium, 791–797, Melbourne.
Tan, Y., Lu, Y., Xu, C.J., Wang, D.L., 2018. Investigation on performance of a large circular pit-in-pit excavation in clay-gravel-cobble mixed strata. Tunnel. Underg. Space Technol. 79, 356–374. https://doi.org/10.1016/j.tust.2018.06.023.
Ting, J., Meachum, L., Rowell, J.D., 1995. Effect of particle shape on the strength and deformation mechanisms of ellipse-shaped granular assemblages. Eng. Computat. 12 (2), 99–108. https://doi.org/10.1108/02644409510799497.
Van den Bergen, G., 1999. A fast and robust GJK implementation for collision detection of convex objects. J. Graphics Tools 4 (2), 7–25. https://doi.org/10.1080/10867651.1999.10487502.
Wang, Z.Y., Wang, L., Zhang, W.G., 2019a. A random angular bend algorithm for two-dimensional discrete modelling of granular materials. Materials 12 (13), 2169. https://doi.org/10.3390/ma12132169.
Wang, J., He, C., Xu, G.W., 2019b. Face stability analysis of EPB shield tunnels in dry granular soils considering dynamic excavation process. J. Geotech. Geoenviron. Eng. 145 (11), 04019092. https://doi.org/10.1061/(ASCE)GT.1943-5606.0002150.
Wittmann, F., Roelfstra, P.E., Sadouki, H., 1985. Simulation and analysis of composite structures. Mater. Sci. Eng. 68 (2), 239–248. https://doi.org/10.1016/0025-5416(85)90413-6.
Zhang, Z.X., Lei, Q.H., 2013. Object-oriented modeling for three-dimensional multi-block systems. Comput. Geotech. 48, 208–227. https://doi.org/10.1016/j.compgeo.2012.07.008.
Zhou, C.H., Zhang, M.M., Li, Y.H., Lu, J.L., Chen, J.Y., 2019. Influence of particle shape on aggregate mixture's performance: DEM results. Road Mater. Pavement Des. 20 (2), 399–413. https://doi.org/10.1080/14680629.2017.1396236.